



Circuits and Systems

Mekelweg 4,
2628 CD Delft
The Netherlands
<https://cas.tudelft.nl/>

CAS-2022-

M.Sc. Thesis

Frequency Domain Joint Estimation of HRF and Stimulus from fUS Data

Yitong Tao

Abstract

To better understand how brain signals are processed and even how the human mind works, analyzing the hemodynamic signal model is one of the most essential steps. In the CUBE group of Erasmus MC, functional ultrasound (fUS) data of a mouse's brain is recorded. By using this fUS dataset, this thesis will solve the problem regarding the joint estimation of hemodynamic response function (HRF) and the underlying stimulus. Usually, hemodynamic responses are investigated in the time domain, while this thesis provides another perspective from frequency domain signal processing.

We consider the hemodynamic response as a convolutive signal mixture, then try to transform it into an instantaneous mixing model by converting the context into the frequency domain. By applying independent vector analysis (IVA), this estimation problem can be solved without facing permutation ambiguity which is a well-known problem regarding independent component analysis (ICA). Additional steps before and after IVA are also discussed so that a whole estimation road map is formed.

Both simulation and experimental analysis are provided to validate this estimation algorithm. Results show that by using this method, both stimulus and HRF estimation can be achieved satisfyingly in a suitable experimental setting. This thesis provides insights and future potentials for IVA to be further investigated in neural signal processing problems.

Frequency Domain Joint Estimation of HRF and Stimulus from fUS Data

THESIS

submitted in partial fulfillment of the
requirements for the degree of

MASTER OF SCIENCE

in

ELECTRICAL ENGINEERING

by

Yitong Tao

This work was performed in:

Circuits and Systems Group
Department of Signals and Systems
Faculty of Electrical Engineering, Mathematics and Computer Science
Delft University of Technology



Delft University of Technology

Copyright © 2022 Circuits and Systems Group
All rights reserved.

DELFT UNIVERSITY OF TECHNOLOGY
DEPARTMENT OF
SIGNALS AND SYSTEMS

The undersigned hereby certify that they have read and recommend to the Faculty of Electrical Engineering, Mathematics and Computer Science for acceptance a thesis entitled “**Frequency Domain Joint Estimation of HRF and Stimulus from fUS Data**” by **Yitong Tao** in partial fulfillment of the requirements for the degree of **Master of Science**.

Dated: 22 Sept. 2022

Chair:

dr. B. Hunyadi

Advisor:

dr. B. Hunyadi

Committee Members:

dr.ir. Richard C. Hendriks

dr. Pieter Kruizinga

Abstract

To better understand how brain signals are processed and even how the human mind works, analyzing the hemodynamic signal model is one of the most essential steps. In the CUBE group of Erasmus MC, functional ultrasound (fUS) data of a mouse's brain is recorded. By using this fUS dataset, this thesis will solve the problem regarding the joint estimation of hemodynamic response function (HRF) and the underlying stimulus. Usually, hemodynamic responses are investigated in the time domain, while this thesis provides another perspective from frequency domain signal processing.

We consider the hemodynamic response as a convolutive signal mixture, then try to transform it into an instantaneous mixing model by converting the context into the frequency domain. By applying independent vector analysis (IVA), this estimation problem can be solved without facing permutation ambiguity which is a well-unknown problem regarding independent component analysis (ICA). Additional steps before and after IVA are also discussed so that a whole estimation road map is formed.

Both simulation and experimental analysis are provided to validate this estimation algorithm. Results show that by using this method, both stimulus and HRF estimation can be achieved satisfyingly in a suitable experimental setting. This thesis provides insights and future potentials for IVA to be further investigated in neural signal processing problems.

Acknowledgments

I would like to start by expressing my sincere gratitude to my supervisor Prof. dr. B. Hunyadi for her invaluable guidance and detailed feedback through the whole period of my thesis research. Our meetings are always delightful and insightful, and make me reflect on my own work every now and then. Her trust and support also encourage me to achieve more than I expected.

Moreover, I'd like to thank dr.ir. Richard C. Hendriks and dr. Pieter Kruizinga for being my thesis committee members. The discussion with dr.ir. Richard C. Hendriks and his research in audio signal processing inspired the proposed method used in this thesis. And dr. Pieter Kruizinga provided me with the fUS dataset which I cannot complete my thesis without. Also, I want to thank PhD students Aybüke Kazaz and Sofia Kotti from CAS group for their enormous help. I'm grateful to your inspiring suggestions along the way, and I want to wish you all the best in your future work and research.

Last but not least, I'd like to thank my friends and family for their love and support in my whole life. I would never be me without you, and I'm happy to share my best moments with you all.

Yitong Tao
Delft, The Netherlands
22 Sept. 2022

Contents

Abstract	v
Acknowledgments	vii
1 Introduction	1
1.1 Thesis Research Question	1
1.2 Thesis Outline	2
2 Background	3
2.1 fUS Imaging Technique	3
2.1.1 Comparison with other techniques	3
2.1.2 PDI Acquisition	3
2.2 Brain Mapping	4
2.3 Hemodynamic Response	5
3 Related Work	7
3.1 Prior Work in Time Domain	7
3.2 Prior Work in Frequency Domain	8
3.3 Prior Work in Audio Signal Estimation	9
4 Methodology	11
4.1 Problem Formulation	11
4.1.1 Signal Modeling	11
4.1.2 Transformation Using STFT	12
4.2 From ICA to IVA	13
4.2.1 ICA	14
4.2.2 Frequency domain ICA and Permutation Problem	14
4.2.3 IVA for Frequency Domain Signal Estimation	15
4.3 Stimulus Estimation	19
4.3.1 Post-IVA Recovery	19
4.3.2 Stimulus Estimation Evaluation	20
4.4 HRF Estimation	21
4.4.1 Simultaneous Method	21
4.4.2 Revised Simultaneous Method	21
4.4.3 Sequential Method	21
4.4.4 HRF Estimation Evaluation	22
4.5 HRF and HTF model	22
5 Simulation Data and Results	23
5.1 Simulation Pipeline	23
5.1.1 Generation Process	24
5.1.2 Stimulus Estimation	25

5.1.3	HRF Estimation	26
5.2	Evaluation	27
5.2.1	Stimulus Estimation Performance	27
5.2.2	HRF Estimation Performance	29
6	Experimental Data and Results	31
6.1	Experimental Pipeline	31
6.1.1	Data Description	31
6.1.2	Data Pre-processing	33
6.1.3	Spatial ICA and Region Selection	34
6.2	Stimulus Estimation	36
6.2.1	Comparison with temporal ICA	36
6.2.2	Source Position Estimation Result	37
6.3	HRF Estimation	38
6.3.1	Evaluation	39
7	Discussion	41
7.1	Answers to Research Questions	41
7.2	Limitations	42
7.3	Future Work	42
8	Conclusion	45

List of Figures

2.1	Coronal Mouse Brain Atlas from Allen Brain Map Database.	5
2.2	Hemodynamic-related signals at a certain brain position.	6
4.1	3-D arrays \mathbf{S} (top left), \mathbf{X} (top right), and \mathbf{H} (bottom)	13
4.2	Observation signals \mathbf{X} and the elemental vector component structure (shown in blue) for IVA.	16
4.3	Assumed neural stimulus waveform. (The total length can be adjusted according to experimental requirements about stimulation duration.)	20
5.1	Simulation Pipeline	23
5.2	Generated HRFs corresponding to each source-observation combination. The $\boldsymbol{\theta}$ parameter sets generated for the 1 st source are: $\boldsymbol{\theta}_1 = [3.0071, 0.7064, 1.7902]$; $\boldsymbol{\theta}_2 = [2.3674, 0.5578, 3.2731]$; $\boldsymbol{\theta}_3 = [6.3406, 0.3134, 4.4608]$. For the 2 nd source: $\boldsymbol{\theta}_1 = [2.8096, 0.0740, 4.4442]$; $\boldsymbol{\theta}_2 = [3.2245, 0.6841, 2.5571]$; $\boldsymbol{\theta}_3 = [3.8848, 0.4024, 3.2672]$	25
5.3	Sources generated for simulation.	25
5.4	Post-IVA recovery by locating peak positions and replacing them with stimulus waveform.	26
5.5	Example estimation results for HTF and HRF	27
5.6	Performance influences by number of stimulus sources.	28
5.7	Performance influenced by number of observations.	29
5.8	Performance influenced by different parameters.	29
6.1	Experimental Pipeline	31
6.2	Stimuli icons in different sizes, shapes, and positions shown on screen.	32
6.3	20 different stimuli vary in position, symbol shape, and size.	33
6.4	Sources with index 4 and 9	34
6.5	Selected parcelization maps and regions after thresholding.	35
6.6	Experiment source estimation	36
6.7	Temporal ICA stimulus peaks estimation results	37
6.8	IVA stimulus peaks estimation results	37
6.9	Performance comparison between IVA and tICA	38
6.10	Estimation results for HTF and HRF	39
6.11	HRF results shown by observation region and stimulus position pairs.	40

List of Tables

5.1	Parameters used in the simulation procedure.	24
5.2	HRF estimation result evaluation in three aspects.	30
6.1	Stimulus Estimation score for different pair of sources.	38

For generations, the human mind has always been a mysterious and exhilarating topic that scientists dedicated countless time and efforts to investigate. One of the key methods to unmask the mystery is by studying brain functional activation signals non-invasively.

Due to the existence of neurovascular coupling (NVC), brain activation in certain regions will cause an increasing requirement of blood flow, and this kind of metabolic response is called hemodynamic response. There are many functional imaging techniques used to capture this response, such as functional magnetic resonance imaging (fMRI) and functional near-infrared spectroscopy (fNIRS). However, regarding the penetration depth for image acquisition as well as spatial and temporal resolution, these methods all have their limitations. In recent years, functional ultrasound (fUS) has emerged as a competitive technology with the potential to be used widely for functional imaging due to its portability, high spatial and temporal resolution, and low cost [1]. However, practical requirements like opening the skull for probing can be a disadvantage for fUS, but it is realizable in a laboratory environment. In this paper, signals collected using fUS will be used for analyzing the hemodynamic response.

To investigate the hemodynamic response in one or more brain regions, a common experimental design is to expose the test object to one or more stimuli, and then record signals from regions of interest. A linear time-invariant (LTI) model is commonly used to model this process, where the impulse response (IR) is called the hemodynamic response function (HRF). Estimating HRF is one of the most essential topics in investigating brain activities because HRF serves as a link between the observed signals and the underlying neural activities. In addition to HRF, the stimulus signal is also of interest to many researchers, as it can be seen as input of the LTI system, and therefore, represents the underlying neural activity. By jointly estimating HRF and stimulus, the brain functional network and the whole cognitive process can be better understood.

Different from many previous works on this similar estimation problem which work in the time domain, this thesis proposes a method performed in the frequency domain. This new perspective exploits the convolutive nature of the observation signal and transforms it into an instantaneous mixing problem at each frequency bin. The proposed method is inspired by a similar mixing model in audio signal processing problems where frequency domain techniques are more widely used.

1.1 Thesis Research Question

This thesis explains how HRF and stimulus are estimated, and the meaning of the results. The main research question can be expressed as three smaller research questions as listed below, which will be solved in this thesis sequentially.

- **RQ1:** How to convert the signal estimation problem into frequency domain?
- **RQ2:** What frequency domain technique can be considered in solving this estimation problem?
- **RQ3:** What neuroscientific insights can the estimation results give?

1.2 Thesis Outline

In this thesis paper, several neuroscientific background topics are introduced in Chapter 2, which are essential to getting into the actual research question itself as well as developing the algorithm. In Chapter 3, previous literature related to HRF and source estimation will be concluded which inspired the formation of this paper. After that, in Chapter 4, the main methods implemented in each step of the estimation procedure are explained. With these methods fully explained, in Chapter 5 the simulation pipeline and corresponding results will be discussed, which investigates the proposed estimation algorithm from a theoretical perspective. Then in Chapter 6, a similar procedure will be used for experimental data which is recorded from a mouse's brain using fUS. Both pipeline steps and results will be explained here, and the results will be compared and evaluated. Chapter 7 discusses existing limitations in the proposed estimation procedure, and also gives several possible directions for future work. Finally, Chapter 8 concludes this paper.

In this chapter, background information about several topics related to neuroscience will be explained in detail. First, functional ultrasound (fUS) is the imaging technique involved in this thesis, and its working mechanism will be explained in Section 2.1. After acquiring fUS imaging data, to further investigate the brain regional response to different stimuli, brain mapping and its relation to the concerned estimation problem will be introduced in Section 2.2. It can also help to explain the experiment result which will be discussed in later chapters. Finally, for a better understanding of the hemodynamic system, Section 2.3 will provide a visual example to explain the relation of the brain, hemodynamic response, stimulus signal, and HRF.

2.1 fUS Imaging Technique

2.1.1 Comparison with other techniques

Techniques like fMRI, fNIRS, and fUS which are used to capture hemodynamic signals share a similar mechanism that depends on the NVC process in the brain. When neural activities happen in a certain brain region, the local blood flow will increase, which gives the possibility to indirectly observe local brain activities by measuring the blood movement.

For fMRI, blood oxygen level-dependent (BOLD) changes are captured using MRI signals when the brain is activated in certain regions. Due to NVC, the concentration change of deoxyhemoglobin which is significantly paramagnetic will influence the local magnetic environment, and it will change the local MRI signal decaying speed [2]. For fNIRS, optical intensity measures are influenced by NVC instead of magnetic field intensity. This technique provides lower spatial resolution compared with fMRI, yet requires lower cost and gives better temporal resolution [3]. For fUS, Power Doppler (PD) signals which come from ultrasound waves reflected back from brain tissues are used to represent cerebral blood volume (CBV) change [4] [5], which will be explained in detail in the next section. Since this indirect representation of neural activity through signal measurements is shared among these techniques, they can also share similar signal processing methods.

2.1.2 PDI Acquisition

Functional ultrasound imaging is based on the Doppler effect of blood cell movement in a certain brain region. When the image acquisition begins, a set of tilted plane waves are sent towards the brain tissue, and the ultrasonic energy scattered back will form images that can be coherently summed into a compound image. This summation step provides better image contrast and resolution, as well as a lower noise level.

However, the resulting compound images contain not only information about blood cell movement, but also other tissues. To only preserve changes due to blood cell movement, a high-pass filter can be applied to compound images over time, which will filter out the influence of tissues that moves slower than blood [6] [7].

After acquiring all the filtered compound images, power Doppler signals can be calculated by averaging across several samples, as shown in equation 2.1 below. At the spatial location (z, x) of the PDI, the pixel value can be calculated as:

$$I(z, x) = \frac{\sum_{j=1}^{N_s} |s_f(z, x, t_j)|^2}{N_s} \quad (2.1)$$

where N_s is the number of filtered compound images for averaging; $s_f(z, x, t_j)$ is the pixel value of corresponding filtered compound image.

The obtained PDI signals are proportional to the CBV of corresponding locations. Therefore, the underlying neural activities can be represented as changing CBV through NVC mechanism, then "translated" into PDI values using fUS imaging technique.

2.2 Brain Mapping

As explained in the previous sections, fUS is the neuro-imaging technique used in this thesis. It can generate spatial maps which match pixel locations to PDI values. Similarly, there are techniques that match biological properties (such as cellular gene expression) and functions (such as memory and cognition) of the brain to spatial regions, which are called (functional) brain mapping [8].

Brain mapping can be considered a generalized form of neuro-imaging. With decades of efforts in brain mapping research, scientists have gathered data and built several successful projects for the human and animal brains, including the Allen Brain Atlas ¹ [9] which will be referred to here. Allen Mouse Brain Atlas matches *in situ* hybridization (ISH) data, which represents DNA or RNA sequence appearance in tissues, with spatial regions in adult mouse brain.

For this thesis, visual stimulus is of concern, therefore visual cortex regions will be investigated in the following parts. Figure 2.1 shows one slice of the Allen Mouse Brain Atlas, which is located around the same position as the experimental data used in this thesis. The visual cortex region is shown as dark green color, which locates on the up-right and up-left corners of this image.

To investigate the regional behavior in the brain regarding visual stimulus, signals from left and right visual cortex regions will be measured and analyzed in this thesis. In this thesis, the regional brain property is represented through HRF, which can be evaluated based on the Divided Visual Field Paradigm: a visual stimulus that appears in the left visual field will lead to visual information projected to the right cerebral hemisphere, and conversely, the visual stimulus appears in the right visual field will be mainly projected to the left cerebral hemisphere [10] [11]. Therefore, the mapping between the left/right visual cortex in the brain and the direction of visual stimulus can be established.

¹Website: <https://mouse.brain-map.org/>

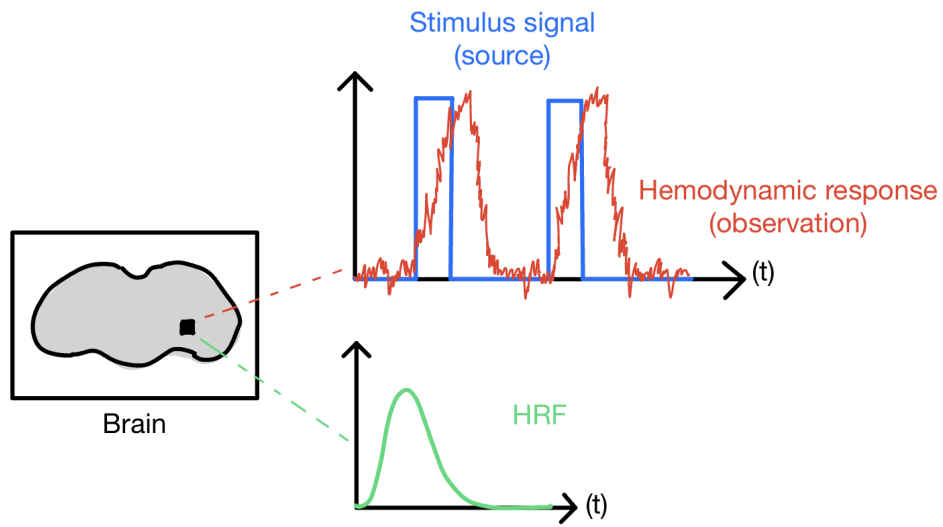


Figure 2.2: Hemodynamic-related signals at a certain brain position.

for each of the source stimuli.

To transfer this signal estimation problem to the frequency domain, a frequency expression of HRF is needed, which is called the hemodynamic transfer function (HTF). The expression of both HRF and HTF will be further explained in Chapter 4.

Functional brain mapping, as well as stimulus and HRF estimation, are among the most concerning research topics in the neuro-signal processing field. This chapter introduces existing literature about this signal estimation problem, as well as its similarity with certain audio signal estimation problems. In Section 3.1, literature focusing on time domain HRF and stimulus analysis will be briefly explained and concluded into several categories. In Section 3.2, several frequency domain approaches which exploit the hemodynamic signal model's convolutive nature will be introduced. Finally, this chapter will end by introducing several audio signal estimation methods that share a similar convolutive model with the current problem. The related works introduced in this chapter can serve as an inspiration that leads to the formation of the estimation method used in this thesis.

3.1 Prior Work in Time Domain

Most of the previous works regarding HRF estimation are based on certain canonical HRF models [13]. These models have a fixed expression and constrained parameters that can be tuned to control signal properties like amplitude, peak delay, etc [14] [15] [16]. By this simplified assumption of HRF signals, different algorithms were proposed to estimate HRF parameters instead of the HRF itself. However, due to the complex and still partly-unknown nature of neural signals, this parameterized method has its limitations. One of the major drawbacks is that one fixed expression cannot adapt to the varying HRF across the whole brain, nor among different stimuli.

To improve the HRF model flexibility and achieve better estimation results, HRF modeling using signal basis sets can also be found in the literature. By linearly combining basis and fitting into the signal model, regression coefficients are estimated which will finally be used to construct an HRF signal. Several well-known signal basis sets are B-splines [17], finite impulse responses (FIR) [18], wavelets [19], and canonical HRF with its derivatives with respect to time and dispersion [20]. This basis signals fitting method is also known as the general linear model (GLM) [21]. HRF estimated using this method can capture more differences across brain regions because it's more flexible compared to the parameter estimation method. Generally, the more basis signals are used, the more reliable and accurate the HRF modeling can be, but it will also lead to the over-fitting problem due to a large degree of freedom [22] [16]. Another limitation is that, since the basis fitting process is based on the statistical model rather than the physical model, the result may not be a faithful representation of the reality which happens in the brain [23].

Another choice to estimate HRF is by using data-driven methods, which don't require a pre-defined HRF shape [24]. By using the data-driven method, the HRF

result is less biased and even more flexible compared with GLM method [25].

In addition to estimating HRF, stimulus estimation is also a popular topic. As previously illustrated in Fig. 2.2, in the hemodynamic model there are three signals of concern. Then by putting noise into consideration, their relation can be expressed as:

$$x = h * s + n \tag{3.1}$$

Here x is the hemodynamic response, h is the HRF, s is the stimulus signal, and n is the additive noise. When estimating h , many previous methods are based on the measured x as well as a known stimulus s , which will not always be available in experiments. Therefore, the requirement of estimating both h and s based on measurement x is of significance during hemodynamic analysis. To achieve this joint estimation of both stimulus and HRF, simplifications are usually applied to the problem. For example, some proposed methods assume the HRF is identical or constrained across brain regions or events [26][16]. Some other methods for joint estimation are only applicable to one-dimension observation data x instead of the whole brain [27] [28].

3.2 Prior Work in Frequency Domain

Though the frequency domain approach is widely used in other signal processing problems, the number of its application in hemodynamic signal estimation is still limited. It is a generally more complex and indirect approach compared with the time domain since it requires additional transformation. However, the frequency domain approach provides the possibility to simplify the signal model from convolution mixture to instantaneous mixture using Fourier transform.

Some literature performs hemodynamic analysis in the frequency domain assuming both observation x and stimulus s are known (using the same symbol as in Eq. 3.1). In [14], HRF is extracted from fMRI by applying the Fourier-wavelet regularised deconvolution (ForWaRD) algorithm in the frequency domain to effectively mitigate the influence of noise. ForWaRD algorithm is a regularisation technique that is used to modify the frequency coefficient after raw HRF estimation by pointwise division. This algorithm also relies on a parametric HRF model. In [29], cross-spectral density functions are calculated for observations x and a fixed stimulus s by using periodograms. And instead of estimating HRF itself, this method provides the total power of all HRFs in the frequency domain as the final result.

When stimulus s is assumed unknown but periodical, frequency domain analysis as discussed in [30] can be applied to a one-dimension observation, single stimulus scenario. This method estimates the underlying correlation structure of hemodynamic response signal by doing spectral density analysis. This method can effectively prevent signal analysis from being affected by high-frequency artifacts.

Due to the small amount of literature that can be referred to regarding frequency domain hemodynamic signal analysis, we'll turn to literature about audio signal processing to find further possibilities to solve this estimation problem.

3.3 Prior Work in Audio Signal Estimation

A popular application field that may share a similar signal model with the concerned joint estimation problem is the audio signal estimation problem. Therefore, methods developed in the audio signal processing literature can be used as a reference to find applicable methods which can be re-implemented for hemodynamic signal estimation.

In the audio signal estimation scenario, several microphones are placed at different positions in a room, and each of them records a version of the displayed source signals. The recording picked up by the microphone experiences reverberation in the room, so the signals can be expressed in a convolutive model similar as Eq. 3.1. Now x represents the audio signal recorded by the microphone, h is the room impulse response (RIR) between one source and one microphone, and s is the displayed source signal. There are two main topics in this audio estimation scenario: blind source separation (BSS) and blind channel identification (BCI). BSS is to estimate source signals s when only the recording signals are known. BCI is to estimate RIR and acoustical transfer functions (ATF), which is the frequency domain expression of RIR, from the recordings.

To realize BSS, one of the most popular methods is by using independent component analysis (ICA), either in the time or frequency domain [31]. This method is usually used when source estimation is the priority since it doesn't give a direct result about channel information. This separation problem is comparable to estimating stimulus signals, therefore ICA in the frequency domain is a potential choice, which will be discussed further in the next chapter.

To perform joint estimation of both source and RIR, second-order statistics can be utilized together with designed cost functions, which turns the estimation problem into an optimization problem [32] [33].

In this chapter, the most essential steps and methods used to model and analyze hemodynamic response signals are discussed in four sections. Section 4.1 will introduce model assumptions for the hemodynamic system, as well as the use of short-time Fourier transform which provides the possibility of moving the research problem to the frequency domain. In section 4.2, the core technique used in the proposed analyzing pipeline, Independent Component Analysis (ICA), and its higher dimensional extension, Independent Vector Analysis (IVA), will be discussed in detail. After implementing IVA in the algorithm, other necessary steps for getting estimations results and evaluation are covered in Sections 4.3 and 4.4, whose results will be shown later in the next chapter. Finally, in section 4.5 the HRF and HTF models will be explained.

4.1 Problem Formulation

4.1.1 Signal Modeling

The signal model assumption for this estimation problem can be expressed as a convolution model as follows, which is an ideal model without considering noise:

$$x_j(t) = \sum_{i=1}^N \sum_{p=0}^{P-1} h_{ji}(p) s_i(t-p) \quad (4.1)$$

Here $x_j(t) \in \mathbb{R}^T$ represents the j^{th} hemodynamic response time sequence (observation), where $j = 1, 2, \dots, M$. Similarly, $s_i(t) \in \mathbb{R}^T$ represents the i^{th} stimulus signal time sequence (source), where $i = 1, 2, \dots, N$. The convolution mixing filter $h_{ji}(p) \in \mathbb{R}^P$ for the j^{th} observation and the i^{th} stimulus, is the corresponding time domain impulse response, which is the HRF with length P .

Alternatively, this convolution model can also be written using the convolution operator:

$$x_j(t) = \sum_{i=1}^N h_{ji}(t) * s_i(t) \quad (4.2)$$

During simulation and experimental signal estimation which will be discussed in later chapters, the presence of noise $v_j(t) \in \mathbb{R}^T$ will be considered, which is assumed to be white and additive. Under this assumption, the model will be written as follows:

$$x_j(t) = \sum_{i=1}^N h_{ji}(t) * s_i(t) + v_j(t) \quad (4.3)$$

In our setting, we assume both HRF and stimulus signals are unknown. Therefore, the research question in the time domain can be interpreted as: *Knowing M observation time series $x_j(t)$, how to find N underlying sources $s_i(t)$ and corresponding mixing filters $h_{ji}(t)$?*

4.1.2 Transformation Using STFT

To convert time series problems to the frequency domain, short-time Fourier transform (STFT) can be used as a powerful tool. It can provide signal frequency domain information that changes over time. For an L -point STFT, using a window function $w(t)$ and with a certain shift length J which creates enough overlap between windows, $x_j(t)$ can be transformed into:

$$x_j^f(k) = \sum_{l=0}^{L-1} w(l)x_j(kJ + l)e^{-j2\pi\omega_f l} \quad (4.4)$$

where $\omega_f = (f - 1)/L$, with $f = 1, 2, \dots, L$ as the frequency.

For a window length L large enough than the length of mixing filter $h_{ji}(p)$ [34], the convolution model expressed in Eq. 4.2 can be transformed into frequency domain by applying STFT on both sources $s_i(t)$ and observations $x_j(t)$. Then the signal model can be rewritten in the frequency domain as:

$$x_j^f(k) = \sum_{i=1}^N h_{ji}^f s_i^f(k) \quad (4.5)$$

here both $x_j^f(k)$ and $s_i^f(k)$ are STFT coefficients of frequency f at the k -th time frame.

The discrete-time notation used here is k , which represents the STFT time frame index, and it will be mostly omitted from the rest of this thesis paper for convenience. For example, random variable x_j^f represents the STFT coefficient at frequency bin f and observation j .

Equation 4.5 can be combined across frequency bins at certain observation j into an array of time series, represented as:

$$\mathbf{x}_j = [x_j^1, \dots, x_j^f, \dots, x_j^F]^T \quad (4.6)$$

Similarly, 4.5 can also be combined across observations at a certain frequency f :

$$\mathbf{x}^f = [x_1^f, \dots, x_j^f, \dots, x_M^f]^T \quad (4.7)$$

Their dimensions are $\mathbf{x}_j \in \mathbb{R}^{F \times K}$ and $\mathbf{x}^f \in \mathbb{R}^{K \times M}$.

Due to the instantaneous mixing nature of signals in each frequency, equation 4.5 can be expressed in matrix form:

$$\mathbf{x}^f = \mathbf{H}^f \mathbf{s}^f \quad (4.8)$$

where $\mathbf{H} \in \mathbb{R}^{M \times N \times F}$ is the 3-D mixing array which stores the values of each Fourier-transformed convolutive filter \mathbf{h}_{ji} together, and \mathbf{H}^f represents the un-mixing matrix at each frequency f , as shown in the bottom sub-image in Figure 4.1.

To combine equation 4.6 and 4.7 further, the 3-D array representation of x_j^f can be written as $\mathbf{X} \in \mathbb{R}^{F \times K \times M}$, as shown in the top-right sub-image of Figure 4.1. Here x_j^f is the elemental entry, and \mathbf{x}_j and \mathbf{x}^f can be seen as 2-D slices inside \mathbf{X} at certain observation j and frequency f , respectively. Similarly, the source signals can also be represented as 3-D array $\mathbf{S} \in \mathbb{R}^{F \times K \times N}$, as the top-left sub-image of Figure 4.1.

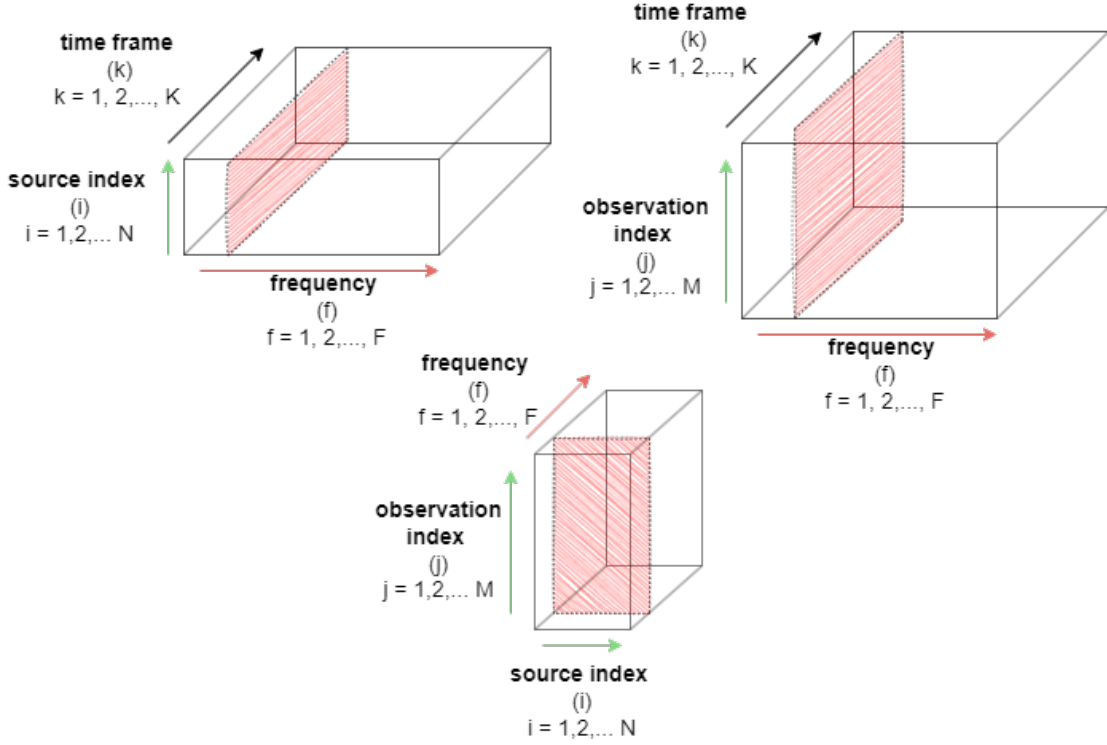


Figure 4.1: 3-D arrays \mathbf{S} (top left), \mathbf{X} (top right), and \mathbf{H} (bottom)

After this step, the research problem can be expressed further as a short-time Fourier estimation problem: *Knowing the observation 3-D array \mathbf{X} , how to estimate the underlying source \mathbf{S} and corresponding system mixing matrix \mathbf{H}^f ?* To make sure this model is solvable, not only the window length L used for STFT should be long enough then the convolutive filter $h_{ji}(p)$, but the equation number should also be larger than the total unknown number in model 4.8, which can be expressed as $N \leq M$.

Compared with equation 4.2 which uses a convolution mixture to represent the problem setting, now equation 4.8 converts the problem into F separated instantaneous mixture estimation problem in the frequency domain. As discussed in Chapter 2, there are plenty of previous applications mainly focusing on audio signal processing sharing a similar signal model with this one, the next research question will be: *which technique can solve this problem?*

4.2 From ICA to IVA

In order to solve Eq. 4.8, the stimulus estimation result can be expressed as:

$$\mathbf{y}^f = \hat{\mathbf{s}}^f = \mathbf{W}^f \mathbf{x}^f \quad (4.9)$$

where $\mathbf{y}^f = \hat{\mathbf{s}}^f$ is the stimulus estimation result, which is a time series vector similar to the expression in Equation 4.7, and \mathbf{W}^f is the un-mixing (separation) matrix with a N -by- M dimension, at frequency bin $f = 1, 2, \dots, F$.

4.2.1 ICA

As introduced in Chapter 3, ICA is a well-known signal processing approach, which can be used to achieve BSS for some audio signal problems. The method assumes signals are mixed instantaneously, and different sources are statistically independent of each other. Although here it cannot be directly applied to the hemodynamic signal model, understanding ICA can still significantly help to explain the methods proposed in this thesis.

To explain how ICA works, here we can assume an instantaneous signal mixing scenario: X is the observation data matrix with M observations and each has T time samples; S is the underlying source data with N independent sources and each has T time samples; A is the mixing matrix where $A \in \mathbb{C}^{N \times M}$. The matrix form of this mixing model can be expressed as:

$$X = A \cdot S \quad (4.10)$$

Since the M observations are measured individually, each observation as a column inside matrix X can be expressed as an instantaneous signal mixture:

$$x_j = \sum_{i=1}^N A_{ji} s_i, \quad j = 1, \dots, M \quad (4.11)$$

The goal of ICA is to separate N statistically independent sources s_i from the mixture. One of the main approaches to achieving this separation is by minimizing the mutual entropy among different sources. There are many ICA algorithms already developed in the literature, like the natural gradient method [35], InfoMax method [36], and FastICA method [37].

Usually, ICA is applied to achieve temporal independence, which means the separated independent sources are time series, this is called temporal independent component analysis (tICA). While for some biomedical applications, when ICA is applied on voxel time series, the goal will change to achieve spatial independence by separating voxel groups (regions). This method is called spatial independent component analysis (sICA) and can be used to detect brain networks [38] [39].

4.2.2 Frequency domain ICA and Permutation Problem

In the current problem, for a fixed frequency f , the signal mixture can be seen as a tICA separation problem. By performing parallel ICA calculations at each frequency bin, the underlying source signals shown in the instantaneous mixing model 4.9 can be estimated as \mathbf{y}^f , and this process can be executed across all frequency bins.

Also, using this ICA model at each frequency f , by calculating the Moore-Penrose pseudo-inverse of \mathbf{W}^f , the corresponding mixing matrix can also be recovered:

$$\hat{\mathbf{H}}^f = (\mathbf{W}^f)^\dagger \quad (4.12)$$

where $\hat{\mathbf{H}}^f \in \mathbb{R}^{M \times N}$ is the HTF estimation result at frequency f . Therefore, theoretically by using ICA on the observation \mathbf{x}^f , desired stimuli and mixing filters can both be estimated.

To get stimulus y_i , all STFT coefficients for the i -th source across frequency bins should be collected for reconstruction. However for each ICA calculation, the resulting un-mixed coefficients y_i^f inside \mathbf{y}^f are in random order regarding source index $i = 1, \dots, N$ across frequency bins. For example, for a $N = 2$ mixture, at frequencies f_0 and f_1 , stimuli estimation after ICA could be in different index order, like:

$$\mathbf{y}^{f_0} = [y_1^{f_0}, y_2^{f_0}]^T \quad \mathbf{y}^{f_1} = [y_2^{f_1}, y_1^{f_1}]^T \quad (4.13)$$

and as a result, if without any additional step, signal reconstruction for each source index will fail. And obviously, a similar random-index problem will also happen for the un-mixing matrix \mathbf{W}^f , due to equation 4.9.

In ICA-related literature, this random-index problem is well-known as permutation ambiguity (PA), where proper grouping algorithms are required to group elements from the same source together, so they can be put into one column and then reconstructed back into a time domain signal.

To solve the permutation ambiguity, previous works have already provided several grouping algorithms involving many different fields of applications, from speech signal which has more additional environment parameters [40], to EEG signals [41] which is similar to the problem being discussed here.

One of the most popular and classic solutions to permutation ambiguity is called the Hungarian algorithm [42], and there are also later approaches developed based on this algorithm dedicated to being applied to different specific scenarios [43]. In this thesis paper, instead of proposing additional grouping algorithms to solve PA, we use another method that prevents permutation from happening in the first place. Compared with adding a grouping algorithm after ICA, this method is simpler and can solve the separation problem and permutation ambiguity at the same time.

4.2.3 IVA for Frequency Domain Signal Estimation

Due to the permutation problem which occurs in the frequency domain ICA algorithm discussed above, another signal independence analysis algorithm is proposed, called independent vector analysis (IVA), which was originally designed for frequency-domain blind source separation problem [44][45][34]. And since IVA inherits ICA's features and also focuses on source separation in noise-free scenarios, in the rest of this chapter, signal model described in Eq. 4.2 will be used, if not specified otherwise.

Instead of calculating independent uni-variate components at each frequency bin, the IVA algorithm treats multi-variate vectors as basic components when doing independence analysis. Figure 4.2 shows the relation between an elemental vector component

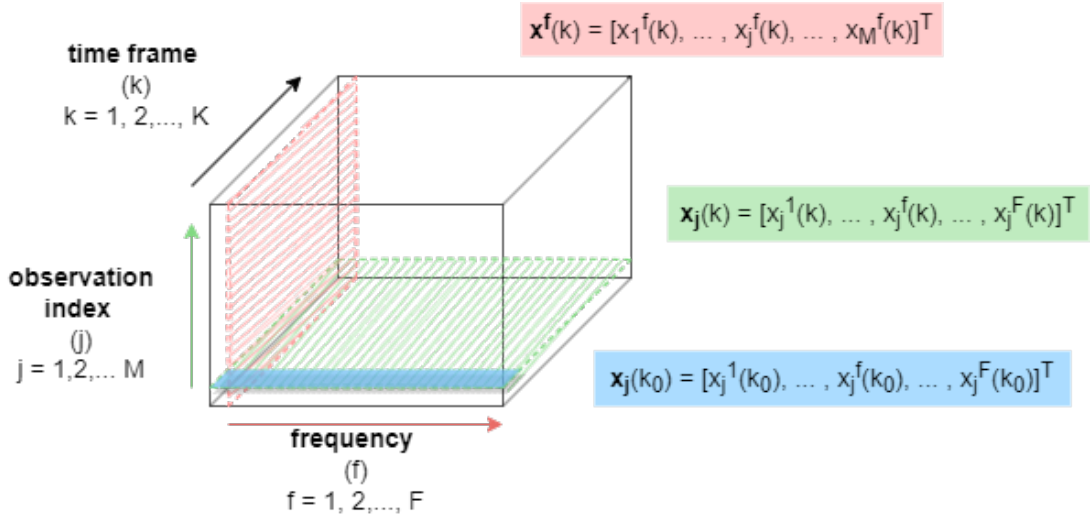


Figure 4.2: Observation signals \mathbf{X} and the elemental vector component structure (shown in blue) for IVA.

$\mathbf{x}_j(k_0)$ and observation \mathbf{X} . (Similar vector expression can be also applied to the target stimulus estimation result \mathbf{Y} , where source number N will replace observation number M).

Therefore, Eq.4.8 can be stacked together across frequency bins and rewritten as the signal mixing model for IVA (# represents element-wise multiplication where matrices are elements):

$$[\mathbf{x}^1, \dots, \mathbf{x}^f, \dots, \mathbf{x}^F]^T = [\mathbf{H}^1, \dots, \mathbf{H}^f, \dots, \mathbf{H}^F]^T \# [\mathbf{s}^1, \dots, \mathbf{s}^f, \dots, \mathbf{s}^F]^T \quad (4.14)$$

Then by combining the entries into 3-D array forms as shown in Fig.4.1, this expression can be simplified into:

$$\mathbf{X} = \mathbf{H} \# \mathbf{S} \quad (4.15)$$

The basic component vector shown in red can be represented as:

$$\mathbf{x}_j(k_0) = [x_j^1(k_0), x_j^2(k_0), \dots, x_j^f(k_0), \dots, x_j^F(k_0)]^T \quad j = 1, 2, \dots, M; \quad k_0 \in [0, K] \quad (4.16)$$

which contains uni-variate components across all F frequency bins at a single time frame k_0 for observation j . In Fig. 4.2, $j = 1$ is used as an example. It is also a temporal element of \mathbf{x}_j as represented in equation 4.6. Using this multi-variate vector of time sequence, the previously mentioned procedure which requires F times ICA calculation can be simplified into one IVA calculation since the information of all frequency bins is concentrated into one elemental vector component.

To achieve both separation of different sources and correct grouping to achieve permutation, there are two corresponding assumptions that the signal mixture model should follow [46]:

- Components of one source are mutually independent with components of another source along time;
- Elements inside one source vector are dependent on the other elements along frequency.

To express this duality in equations, an objective function can be defined using the definition of mutual information among different vectors, here interpreted as different sources. Kullback-Leiber divergence between two functions is used to calculate this mutual information (dependency):

$$\begin{aligned}
\mathcal{C} = \mathcal{I}(\mathbf{Y}) &= \mathcal{KL}\left(p(\mathbf{y}_1, \mathbf{y}_2, \dots, \mathbf{y}_N) \parallel \prod_i^N q(\mathbf{y}_i)\right) \\
&= \int p(\mathbf{y}_1, \mathbf{y}_2, \dots, \mathbf{y}_N) \log \frac{p(\mathbf{y}_1, \mathbf{y}_2, \dots, \mathbf{y}_N)}{\prod_i^N q(\mathbf{y}_i)} d\mathbf{y}_1 \dots d\mathbf{y}_N \\
&= \int p(\mathbf{x}_1, \mathbf{x}_2, \dots, \mathbf{x}_M) \log p(\mathbf{x}_1, \mathbf{x}_2, \dots, \mathbf{x}_M) d\mathbf{x}_1 \dots d\mathbf{x}_M - \sum_{f=1}^F \log |\det \mathbf{W}^f| \quad (4.17) \\
&\quad - \sum_{i=1}^N \int p(\mathbf{y}_i) \log q(\mathbf{y}_i) d\mathbf{y}_i \\
&= \text{const.} - \sum_{f=1}^F \log |\det \mathbf{W}^f| - \sum_{i=1}^N E[\log q(\mathbf{y}_i)]
\end{aligned}$$

The first function $p(\mathbf{y}_1, \mathbf{y}_2, \dots, \mathbf{y}_N)$ is the joint probability density function (PDF) of all sources, and the second function $\prod_i^N q(\mathbf{y}_i)$ is the product of marginal PDFs of each source as multi-variate time sequence. The constant term in the final step comes from the definition of \mathbf{x}_j 's entropy $H(\mathbf{x}_j)$, which is already known. By using the equation 4.9, we can express \mathbf{Y} into observations \mathbf{X} and mixing matrix \mathbf{W}^f as: $\mathbf{y}^f = \mathbf{W}^f \mathbf{x}^f$. By assuming this process zero-mean and spatially white, rows of the un-mixing matrix \mathbf{W}^f are orthogonal, therefore $\sum_{f=1}^F \log |\det \mathbf{W}^f| = 0$.

Now equation 4.17 can be simplified into:

$$\mathcal{C} = \text{const.} - \sum_{i=1}^N E[\log q(\mathbf{y}_i)] \quad (4.18)$$

By using the definition of entropy again, equation 4.18 can be expressed as:

$$\mathcal{C} = \text{const.} + \sum_{i=1}^N H(\mathbf{y}_i) = \text{const.} + \sum_{i=1}^N \left(\sum_{f=1}^F H(y_i^f) - \mathcal{I}(\mathbf{y}_i) \right) \quad (4.19)$$

which is due to the relation $H(\mathbf{y}_i) = \sum_{f=1}^F H(y_i^f) - \mathcal{I}(\mathbf{y}_i)$.

From equation 4.19, to achieve $\min(\mathcal{C})$, it's equivalent to $\min(\sum_{f=1}^F H(y_i^f))$ and $\max(\mathcal{I}(\mathbf{y}_i))$. In other words, the goal of finding mutually independent sources comes

together with maximizing the mutual information of elements within each source vector. This conclusion proves the two assumptions are both valid for solving the IVA problem.

The detailed steps in the IVA algorithm will be provided in the following parts, which are similar to traditional ICA in general, but with multi-variate variables instead of uni-variate variables, and therefore, each step will also be a multi-variate version¹.

4.2.3.1 IVA Preparation

For each frequency f , perform zero-mean on \mathbf{x}^f by subtracting mean values along time:

$$\mathbf{x}_{zero-mean}^f = \mathbf{x}^f - E_K[\mathbf{x}^f] \quad (4.20)$$

Then by doing principle component analysis (PCA) at each frequency, data is whitened and the dimension M is reduced to N , making the following parts an N -to- N un-mixing problem. The final result of this preparation step is \mathbf{z}^f :

$$\mathbf{z}^f = \mathbf{Q}\mathbf{x}_{zero-mean}^f, \quad (\mathbf{Q} = \mathbf{D}^{-1/2}\mathbf{E}^H) \quad (4.21)$$

where \mathbf{Q} is a linear transformation matrix, with $\mathbf{D} = \text{diag}(\lambda_1, \dots, \lambda_N)$ the diagonal matrix of the first N largest eigenvalues of spatial correlation matrix $\mathbf{R} = \mathbf{x}_{zero-mean}^f[\mathbf{x}_{zero-mean}^f]^H$, and $\mathbf{E} = [\mathbf{e}_1, \dots, \mathbf{e}_N]$ which is matrix of their corresponding eigenvectors.

4.2.3.2 Learning Algorithm - Natural Gradient Method

According to equation 4.18, which is the cost function of this dependency minimization problem, we can differentiate the cost function calculated from \mathbf{z}^f with respect to the un-mixing matrix, to find the one which can achieve the lowest cost:

$$\Delta\mathbf{W}^f \propto \frac{\partial\mathcal{C}}{\partial\mathbf{W}^f} \cdot (\mathbf{W}^f)^T\mathbf{W}^f \quad (4.22)$$

where $(\mathbf{W}^f)^T\mathbf{W}^f$ is the scaling matrices. Then the gradient learning rule can be expressed as:

$$\Delta\mathbf{W}^f = \{\mathbf{I} - \mathbf{E}[\phi(\mathbf{y}^f) \cdot \mathbf{y}^{fH}]\} \cdot \mathbf{W}^f \quad (4.23)$$

$$\mathbf{W}^f \leftarrow \mathbf{W}^f + \eta \cdot \Delta\mathbf{W}^f \quad (4.24)$$

where $\phi(\mathbf{y}^f)$ is a multivariate nonlinear score function, and η is the learning rate. When the value difference between two iterations is smaller than a certain threshold, this iteration algorithm stops and outputs \mathbf{W} with \mathbf{y}_i .

To find a suitable score function $\phi(\mathbf{y}^f)$, first we can express it as a vector:

$$\phi(\mathbf{y}^f) = [\phi(\mathbf{y}_1^f) \quad \dots \quad \phi(\mathbf{y}_N^f)]^T \quad (4.25)$$

and for each entry, the nonlinear function can be related to its source prior PDF across frequency.

¹The algorithm described below is partly based on the Matlab code provided by: <https://github.com/teradepth/iva>

According to [34], experiments on audio signals indicate that super-Gaussian distribution is a suitable choice to represent its frequency domain source prior PDF. Therefore, for simplicity, here we also assume super-Gaussian distribution for stimuli in this experiment. So the source prior can be expressed as a dependent multivariate super-Gaussian distribution as in [34]:

$$\phi(\mathbf{y}_i^f) = -\frac{\partial \log[q(\mathbf{y}_i^{[1]}, \dots, \mathbf{y}_i^{[F]})]}{\partial \mathbf{y}_i^{[f]}} = \frac{\mathbf{y}_i^{[f]}}{\sqrt{\sum_{b=1}^F |\mathbf{y}_i^{[b]}|^2}} \quad (4.26)$$

4.2.3.3 IVA Reconstruction

After getting un-mixing matrix \mathbf{W}^f from Equation 4.24, we can restore the original dimension using matrix \mathbf{Q} . After that, the scaling ambiguity can be solved by adjusting the separation matrix:

$$\mathbf{W}_{norm}^f = \text{diag}((\mathbf{W}^f)^{-1})\mathbf{W}^f \quad (4.27)$$

Then by using equation 4.9, the separated source \mathbf{y}^f as well as 3-D array \mathbf{Y} can be obtained. After that, by performing inverse-STFT (ISTFT) on \mathbf{Y} using the same parameters as STFT before, we can finally find the separated stimuli time sequences $y_i(t) = \hat{s}_i(t), i = 1, 2, \dots, N$.

4.3 Stimulus Estimation

4.3.1 Post-IVA Recovery

Ideally, the source estimation results from the IVA algorithm should be the true stimuli. However, due to model inaccuracy and estimation errors, the results cannot be reconstructed perfectly. For this research problem, since the sources are neural stimuli sequences, their unique shape can be taken advantage of. Their shapes are similar to impulse trains but with several seconds of activation duration for each impulse and a certain pattern of rest time in between.

This unique source sequence shape will cause the IVA estimation results to be spiky in the time domain, with several peaks representing potential activation moments. Using this information, we can better reconstruct the source stimuli by locating when activation happens on the time axis, then applying a certain signal waveform to it.

In the estimation algorithm, a MATLAB function *findpeak()* is used to provide peak locations and corresponding height values. In order to find at which time point stimuli happen, this function can take several configurable parameters and constrain which local maximums in the signal should be counted as reasonable peaks: the minimum peak value, the minimum distance between two peaks, the total number of peaks, etc. Which parameters are configurable depends on the actual experimental setting, and more determined information will lead to a more accurate estimation result.

After finding all activation moments, an activation waveform can be applied to all the moments to mimic the neural activation incidence. The neural activation waveform is usually modeled as a smoother shape compared with a square wave [47], so here we use two exponential curves, as shown in Figure 4.3. After inserting all the activation

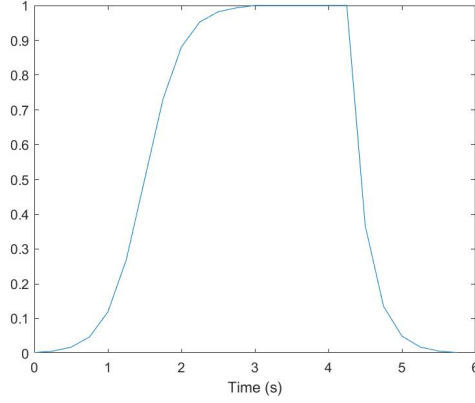


Figure 4.3: Assumed neural stimulus waveform. (The total length can be adjusted according to experimental requirements about stimulation duration.)

time points with the waveform, the output time sequence can be seen as the final stimulus estimation result.

4.3.2 Stimulus Estimation Evaluation

There are two source evaluation methods that are applicable in this thesis paper, with their own different features and usages. In the following two equations 4.28 and 4.29, we assume the estimated sequence is represented as y and the real sequence as s .

(1) The first evaluation method is using normalized cross-correlation between the estimated source and the real source sequence, which will be equal to 1 at zero lag when two sequences are exactly the same (in this case it's an auto-correlation):

$$\hat{\mathbf{R}}_{ys,norm}(m) = \frac{1}{\sqrt{\hat{\mathbf{R}}_{yy}(0)\hat{\mathbf{R}}_{ss}(0)}}\hat{\mathbf{R}}_{ys}(m) \quad (4.28)$$

(2) The second evaluation method is quantifying signals into discrete stimulus events and calculating the event appearance correctness. This method is simpler compared to the first one but requires setting a period within which the estimated stimulus appearance can be considered a "hit". By using the Kronecker Delta function, this method can be expressed as:

$$\mathcal{KD}_{avg}(y, s) = \frac{1}{P} \sum_{p=1}^P \delta(y(p), s(p)) \quad (4.29)$$

where $p = 1, 2, \dots, P$ is the index of a stimulus event, and P is the total number of stimulus events in one source signal.

4.4 HRF Estimation

4.4.1 Simultaneous Method

From the IVA algorithm described in Section 4.2, IVA final results contain not only the estimated source time sequence $\hat{s}_i(t)$, but also un-mixing matrices \mathbf{W}^f at each frequency f . From equation 4.12 we know that hemodynamic transfer function (HTF), which represents the frequency domain transformed HRF, can be derived directly from \mathbf{W}^f as $\hat{\mathbf{H}}^f = (\mathbf{W}^f)^\dagger$. So theoretically, each $h_{ji}(p)$ can be estimated by applying ISTFT to the vector $\hat{\mathbf{h}}_{ji}$ which contain frequency elements with same observation index j and source index i .

4.4.2 Revised Simultaneous Method

To improve the result of the simultaneous method, this revised method modifies the IVA algorithm used in the previous steps. At the end of each iteration of updating \mathbf{W} , first calculate temporary mixing matrices $\mathbf{A}^f = (\mathbf{W}^f)^\dagger$ for each f , then stack them back into 3-D array \mathbf{A} in the same order as \mathbf{W} . As the canon HTF model will be known as equation 4.31, then each column \mathbf{a}_{ji} is fitted to the HTF model and outputted together as $\hat{\mathbf{A}}$. Finally, calculate the un-mixing matrices back by $\mathbf{W}_{rev}^f = (\hat{\mathbf{A}}^f)^\dagger$, and use them to proceed to the next iteration.

Revising the IVA algorithm by utilizing the HTF model information can restrain each column in the mixing 3-D array \mathbf{A} to be more canonical, iteration by iteration. Therefore, IVA can not only find a fixed mixing pattern between observation positions and sources but also make this mixing filter converge to an HTF-shaped signal. This revised algorithm will also influence stimuli estimation performance.

However, because the error in IVA stimuli estimation results compared with real stimuli cannot be avoided, the HTF information is also affected, and unlike source sequence estimation, the error in HTF cannot be compensated by using additional steps like the peak-finding process. So practically, HRF estimation achieved by using direct IVA results will lead to large errors, making this revised method also inappropriate to actual data.

4.4.3 Sequential Method

To estimated HRF, the already achieved stimulus estimation results $\hat{s}_i(t)$ can be used together with observation signals $x_i(t)$. In this way, the HRF estimation can only happen after stimulus estimation, which leads to this sequential method.

By using equation 4.8 where both \mathbf{X} and \mathbf{S} are known either by given or by the previous estimation, we can calculate the deconvolution problem directly from this equation. Besides, as the canonical HTF shape can also be known from previous literature, it can be used to reshape the estimation result, the detailed steps will be discussed in the next chapter.

4.4.4 HRF Estimation Evaluation

The evaluation of HRF can come from two aspects:

1. The statistical accuracy of estimated HRF signal shape compared with the real HRF signal, which is similar to stimulus evaluation criteria;
2. The neural scientific meaningfulness of HRF estimation results, represented by HRF-related parameters' regional and stimulus-wise behavior.

The first one can be applied to the simulation result since real HRFs (ground truth) are manually generated, therefore, can be known and used for evaluation. However, for experimental estimation, there's no real HRF signal to be known, so the related parameters (e.g. amplitude value, peak delay, total length,...) of HRF can be used to evaluate the estimation performance. As already discussed in Chapter 2, one of the most significant patterns regarding HRF regional behavior with respect to different visual stimuli is that the left visual-related brain region will respond to visual stimuli appearing on the right more significantly, and vice versa. By using this pattern, we can use only the amplitude value of each HRF signal to evaluate HRF estimation results. The detailed evaluation results will be given in the next two chapters.

4.5 HRF and HTF model

Although in this thesis, the stimulus and HRF estimation algorithm is not based on canonical HRF/HTF models, they will be used during the fitting procedure and in some future improvements. Therefore, this section will introduce the Gamma models for HRF and HTF which are used in this thesis.

As mentioned in the previous chapter, the hemodynamic process is usually modeled as an LTI system. HRF is the system's impulse response and is usually described using Gamma functions in many previous researches [15][22][48]. Here to further simplify the expression, a three-parameters canonical model with one Gamma function can be used to express HRF shape [49] :

$$f(t, \boldsymbol{\theta}) = \theta_1 (\Gamma(\theta_2))^{-1} \theta_3^{\theta_2} t^{\theta_2-1} e^{-\theta_3 t} \quad (4.30)$$

Since the goal of this thesis paper is to analyze the hemodynamic process in the frequency domain, a frequency domain HRF model should also be generated. By applying Fourier transform to Equation 4.30, we can derive the canonical hemodynamic transfer function (HTF) as ²:

$$\mathcal{F}\{f(t, \boldsymbol{\theta})\} = \theta_1 \theta_3^{\theta_2} (\theta_3 + j2\pi f)^{-\theta_2} \quad (4.31)$$

In this thesis, equation 4.31 will be used for fitting estimated HTF results, which can give a more meaningful HRF signal shape after being transformed back to the time domain for evaluation.

²This HTF expression is developed by ir. S.E. Kotti, PhD student in Circuits and Systems (CAS) group, TU Delft.

Simulation Data and Results

In the previous chapter, most of the major techniques used in the proposed algorithm are introduced. To test the algorithm's performance using artificially generated data, a simulation is designed which will be explained in this chapter. In Section 5.1, a pipeline that describes how signals are generated and estimated will be explained with example inputs and outputs. Then in 5.2, the estimation results will be evaluated and the influence of changing different parameters will be explained.

5.1 Simulation Pipeline

The simulation assumes the scenario as: N stimulus time sequences (sources) are fed into the signal model, and M observation time sequences (observations) are recorded from positions that have distinguished characteristics regarding their responses to stimuli. One source consists of a fixed number P of stimuli with a certain shape, and every two adjacent stimuli are separated by a resting time t_r which is randomized in values. The task of the estimation algorithm is to recover N sources and $(N \times M)$ corresponding HRFs from the known M observations.

Figure 5.1 shows the main steps of simulation, which consists of a *Generation Process*, which outputs artificial observation time sequences, and the following steps for signal estimation. The main variables passed between steps are also annotated in the diagram.

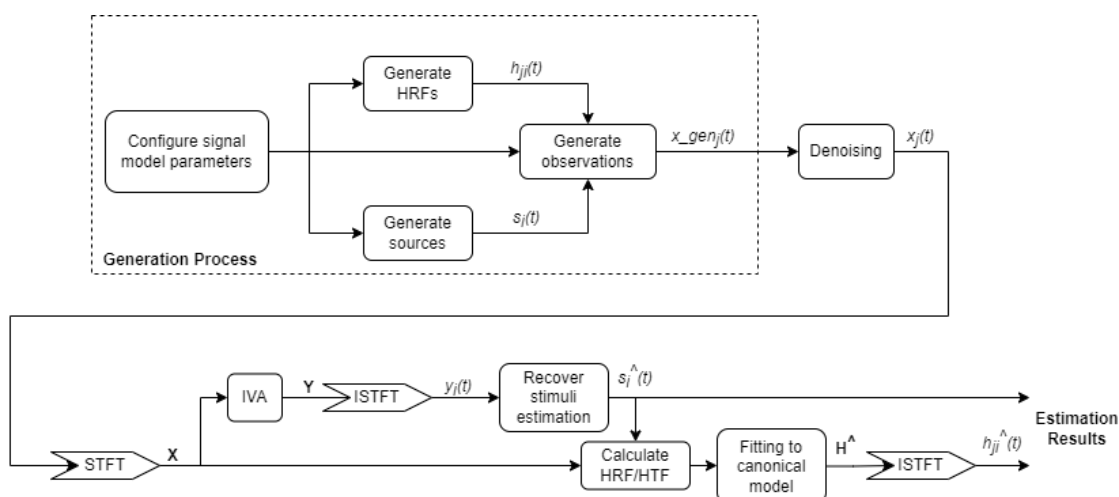


Figure 5.1: Simulation Pipeline

5.1.1 Generation Process

Before generating any signals, the algorithm should first **configure signal model parameters**. In this step several important parameters will be set: fUS sampling rate F_s which is close to the rate used in the actual experiment; source number N and observation number M which should satisfy $N \leq M$; randomized resting duration's maximum and minimum values $[t_{r,min}, t_{r,max}]$ between two stimuli; stimulus duration which is constant for all sources; the total number of stimuli P in one source; duration of HRFs; window length L used in STFT which should be longer than HRFs' duration; SNR for additive white noise.

As an example for this simulation, the values in Table 5.1 are used. All the results and plots shown in the rest of this chapter will use this set of parameter values, if not specified otherwise.

Table 5.1: Parameters used in the simulation procedure.

Simulation Parameters	
F_s	4 [Hz]
N	2
M	3
$t_{r,min}$	5 [s]
$t_{r,max}$	20 [s]
stimulus duration	3 [s]
P	10
HRF duration	15 [s]
window length L	20 [s]
SNR	10 [dB]

After configuring all the parameters needed for the simulation, the next step is to **generate HRFs**, which are treated as ground truth in the simulation. By using the Gamma HRF model shown in Equation 4.30, three model parameters $[\theta_1, \theta_2, \theta_3]$ are needed for each observation-source pair and used to construct corresponding HRF as a time sequence with a duration of 15s. Figure 5.2 below shows the HRFs used in this simulation.

To **generate sources** according to the setting mentioned above, we concatenate P identical pieces of stimuli into a time sequence, with a randomized rest time $t_r \in [t_{r,min}, t_{r,max}]$ between every two adjacent stimuli, and this process repeats for both sources we need. The stimulus waveform is the same as Figure 4.3, with a 3s duration above half-peak value (which is 0.5 here). The $N = 2$ sources are statistically independent from each other, and their appearances in time domain is also random, as shown in Figure 5.3.

The final step in *Generation Process* is to **generate observations**, which will be output as $x_{gen,j}(t)$ to the next step. This generation step takes HRFs $h_{ji}(t)$ and sources $s_i(t)$ from the previous two steps as input, where $i = 1, 2$ and $j = 1, 2, 3$. By using the signal model in equation 4.3, HRFs are convolved with corresponding sources and summed into observations, then each observation is added to their corresponding white

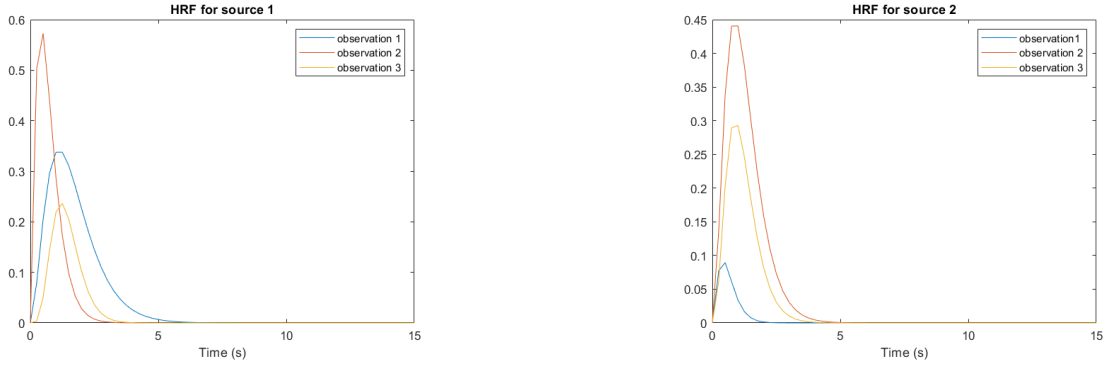


Figure 5.2: Generated HRFs corresponding to each source-observation combination. The θ parameter sets generated for the 1st source are: $\theta_1 = [3.0071, 0.7064, 1.7902]$; $\theta_2 = [2.3674, 0.5578, 3.2731]$; $\theta_3 = [6.3406, 0.3134, 4.4608]$. For the 2nd source: $\theta_1 = [2.8096, 0.0740, 4.4442]$; $\theta_2 = [3.2245, 0.6841, 2.5571]$; $\theta_3 = [3.8848, 0.4024, 3.2672]$.

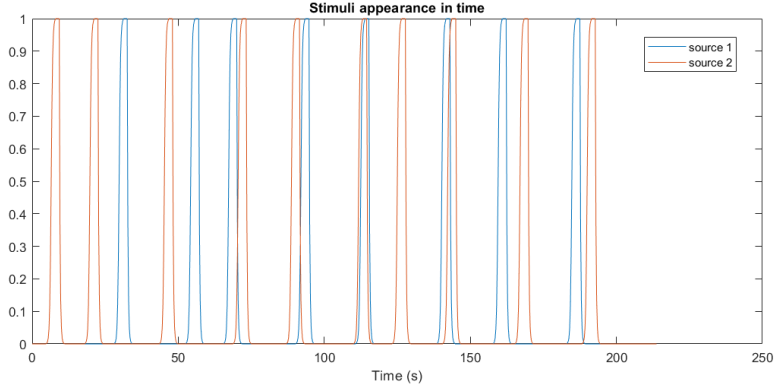


Figure 5.3: Sources generated for simulation.

noise sequence based on its signal power and $SNR = \frac{S_{signal}}{S_{noise}}$. This generated observation time sequence is an artificial version of the recorded fUS signal, and therefore, will be given to the following estimation procedure as initial input.

5.1.2 Stimulus Estimation

The first step of estimation process is **denoising** with a low-pass filter which has cut-off frequency at 0.2 [Hz][49]. This step filters out high-frequency artifacts in observations, by using the information that hemodynamic response signals mostly contain information in a higher frequency range. The output of this step is $x_j(t)$, which corresponds to the one in equation 4.2.

To transform $x_j(t)$ into the frequency domain, STFT is applied as explained in Section 4.1.2, which gives 3-D array \mathbf{X} as output which is applicable for IVA in the next step. This \mathbf{X} will also be used in later steps to calculate HRF.

After deriving the 3-D array \mathbf{X} , **IVA** can be implemented to estimate the underlying sources, as discussed in detail in Section 4.2.3. The outcome of IVA \mathbf{Y} is also a 3-

D array representation of estimated sources. Then after ISTFT, the estimated time domain source sequences are derived as $y_i(t)$.

As the last step to get the final stimuli estimation result, a **post-IVA recovery** is needed as already stated in Section 4.3.1. This recovery process can be visualized as Figure 5.4, where blue signals are estimated sources $y_i(t)$ by IVA, red circles indicate which peak will be recovered as the estimated stimulus, and yellow signals are scaled true stimuli for easier comparison. Then after applying the stimulus waveform at each peak time point, the estimated source sequences $\hat{s}_i(t)$ are comparable to the known real sources $s_i(t)$, therefore can be evaluated using the method mentioned in Section 4.3.2. For this example, the cross-correlation evaluation gives a score of 0.8762, and the discrete score is 0.85.

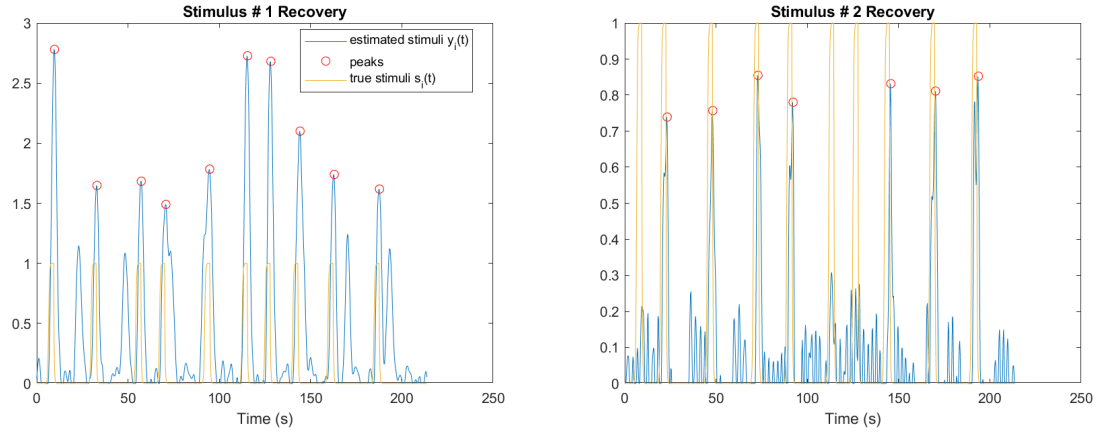


Figure 5.4: Post-IVA recovery by locating peak positions and replacing them with stimulus waveform.

5.1.3 HRF Estimation

After acquiring \mathbf{X} and $\hat{s}_i(t)$, we can **calculate HRF** by first transforming $\hat{s}_i(t)$ into a time-frequency domain 3-D array $\hat{\mathbf{S}}$, then by using the signal model described in Eq. 4.14, frequency domain HTF can be directly calculated using the *Sequential Method* as described in Section 4.4.3, and easily transformed into HRF results.

However, the estimated HTF/HRF result now may have a distorted shape due to the influence of system error, remaining noise, or model inaccuracy. To get an HRF result resembling the canonical shape, an additional **fitting** step is required before the final ISTFT. Each HTF result is fitted into the canonical HTF model as shown in equation 4.31 by solving the following optimization problem:

$$\begin{aligned} & \min_{\theta_1, \theta_2, \theta_3} \|\Delta f(t, \boldsymbol{\theta})\|_2^2 \\ & = \min_{\theta_1, \theta_2, \theta_3} [\text{Re}\{\|\mathcal{F}\{f(t, \boldsymbol{\theta})\} - HTF_{estm}\|_2^2\} + \text{Im}\{\|\mathcal{F}\{f(t, \boldsymbol{\theta})\} - HTF_{estm}\|_2^2\}] \end{aligned} \quad (5.1)$$

where HTF_{estm} represents the raw HTF estimation result as described in Section 4.4.3 waiting to be fitted, and $\mathcal{F}\{f(t, \boldsymbol{\theta})\}$ represents the signal model with $\boldsymbol{\theta}$ to be estimated, which has the same length as HTF_{estm} .

In this optimization problem, three parameters in $\boldsymbol{\theta}$ are derived which can minimize the cost function f . Since the HRF model shares the same set of parameters as the HTF model, by feeding $\boldsymbol{\theta}$ back into the HRF signal model, we can have the final fitted HRF result. Figure 5.5 shows one of the results (h_{22} : 2nd observation's HTF/HRF to the 2nd stimulus) of our example. The left plot is the HTF result, and the right one is the HRF result. The blue line represents the true HTF/HRF previously generated in Figure 5.2a; the red line represents the result without fitting; while the yellow line is the final fitted result. From the plots, we can see that the final result is close to the ground truth, and the fitting tuned the result towards a more canon-like shape without too much compromising the estimation performance.

For HRF, peak value (amplitude) and peak delay in time are the two most essential parameters. In this example, the fitted HRF result has a better peak value compared with the raw result, with only a 1.75% relative error. However, the peak delay of fitted HRF is a little worse than raw HRF. Since this only shows one example among 6 HRF results, the estimation performance regarding peak value and peak delay will be further discussed in the next section.

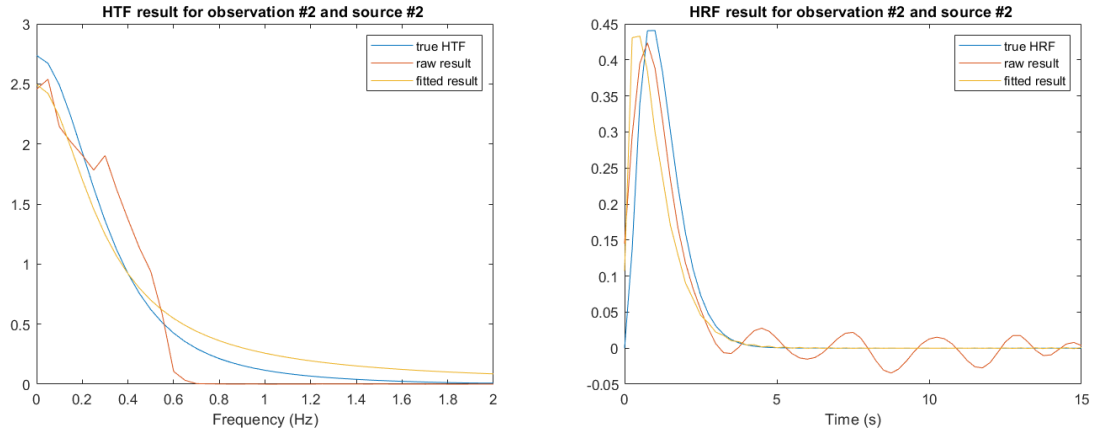


Figure 5.5: Example estimation results for HTF and HRF

5.2 Evaluation

5.2.1 Stimulus Estimation Performance

As mentioned in Section 4.3.2, there are two methods for source evaluation. The cross-correlation method as expressed in Eq. 4.28 gives the similarity between the estimated source signal and the true source signal, and therefore, it's more accurate than the second one which treats each stimulus as a discrete instance. As a result, in this section, only the first method is used, if not specified otherwise.

As discussed in Table 5.1, there are 10 related parameters in this simulation, among which some are configurable. To investigate how stimulus estimation performance will change in different scenarios, the stimulus estimation score can be plotted versus several parameters of interest. And by analysing these parameters' influence to the performance, suggestions towards future experimental design can be concluded. In this section, every data point in all the following figures are calculated by averaging the performance score of 5 trials where source signals and HRFs are randomly generated, using the same set of parameters. The error bar indicated the standard deviations of each set of data. And for each plot, the parameter of interest will change, and other parameters remain the same.

Figure 5.6 below shows that with a fixed number of observations (here $M = 15$), increasing **source number** N can lead to a gradually decrease performance. This is easy to understand because it's equivalent to increasing the number of unknowns while the given information is fixed.

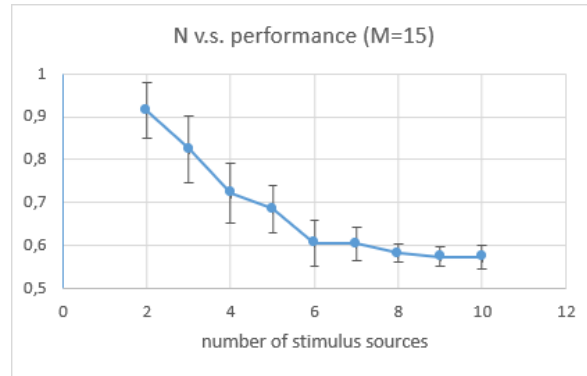


Figure 5.6: Performance influences by number of stimulus sources.

Figure 5.7a and 5.7b below show the influence of increasing **observation number** M . With a fixed number of stimuli, when more observations are known, theoretically the performance will be better. However, from the figures we can see that the performance is not significantly relevant to this change. This result may due to the PCA process inside IVA algorithm, where dimension reduction is applied. When more observation is known to the algorithm, this step will reduce more information which leads to a compensation towards the final result. Also, the plots shown that the trials has a relatively high variance, therefore the result may also be influenced by randomness.

By concluding findings in Fig. 5.6 and Fig. 5.7, the experimental design suggestion is: set a small number of sources as estimation target, and record smaller number of observation signals for a shorter computation cost.

Figure 5.8a shows how performance will change when maximum rest duration between two activation $t_{r,max}$ increases. It can be concluded that a longer possible rest duration upper bound can lead to a better separation performance. Figure 5.8b shows when the possibility duration of rest time is fixed to be 10s, how rest time length in general can influence the performance. We can conclude from the plot that the performance is not significantly influenced by the general rest time. However, in real experiments, the total rest duration will be restricted by practical limitations and cannot be too

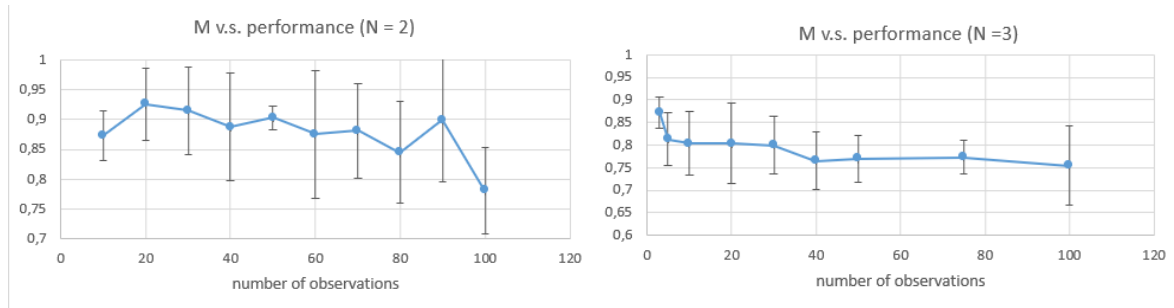


Figure 5.7: Performance influenced by number of observations.

long.

By concluding Fig. 5.8a and 5.8b, the experimental design suggestion is: give a larger range of possibility for rest time, and keep the total rest duration within a reasonable length.

Finally, in Fig. 5.8c, the influence of noise level is shown. A higher SNR level will lead to a better estimation performance, which is as expected.

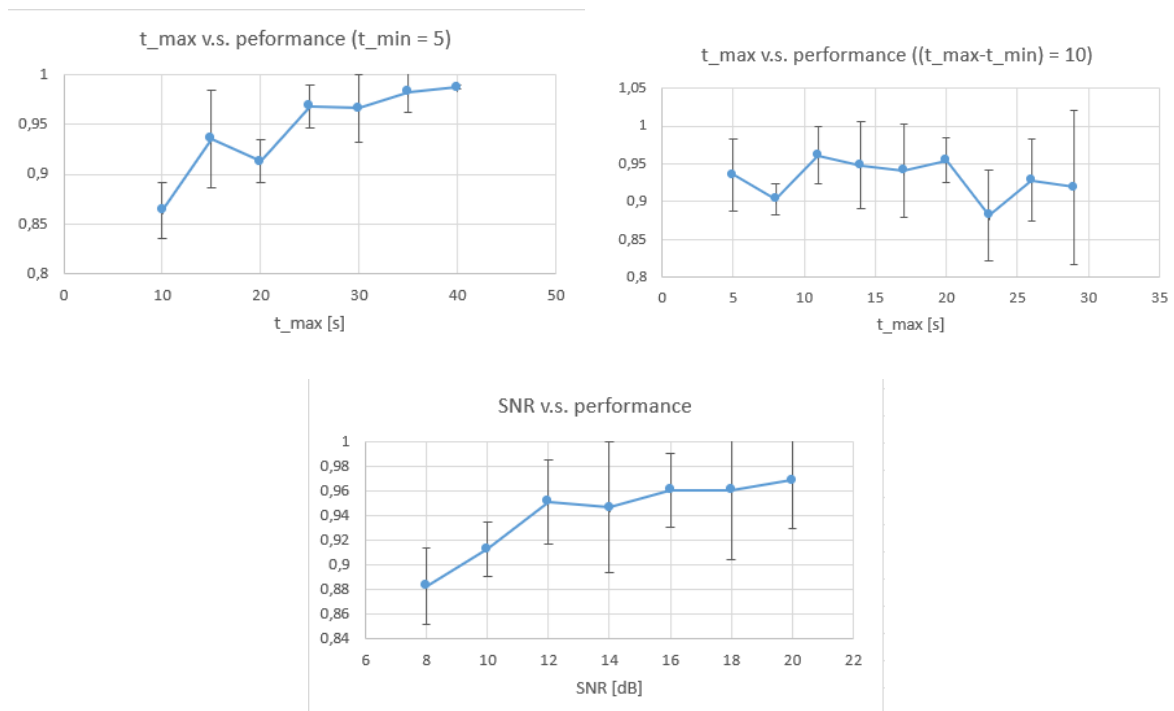


Figure 5.8: Performance influenced by different parameters.

5.2.2 HRF Estimation Performance

In this section, HRF estimation results for the example will be evaluated in three aspects: amplitude, peak delay, and the whole HRF. Performance of these aspects can

be quantified as: amplitude relative error measured in %, $\Delta(\text{Peak delay})$ measured in seconds, and signal mean square error (MSE), respectively.

In this example, there are 6 HRF results in total, each corresponding to one pair of observation and source signals. In the following Table 5.2, each aspect is calculated as the average of all 6 results, which represents the performance in general.

Table 5.2: HRF estimation result evaluation in three aspects.

HRF Evaluation	
Amplitude relative error	14.8 %
$\Delta(\text{Peak delay})$	0.33 [s]
<i>MSE</i>	0.0012

For the amplitude value, the estimated result is very near the true HRF in most cases. The average error between estimated amplitude and true amplitude is around 15%, which is on an acceptable level. The fitting process sometimes may reduce the amplitude error compared with the raw HRF, as shown in Fig. 5.5. However, it is not always guaranteed. For the peak delay, the difference between estimated HRF and true HRF is around 0.33s on average. Compared with the 15s duration of HRF, this error is very small. Similar to amplitude value, the fitting process is not always helping with reducing the error. The averaged MSE of the HRF estimation has a value of 0.0012, which means in this example, the estimated HRF is very similar to the true ones.

The HRF estimation performance can also be influenced by changing model parameters listed in Table 5.1, which is similar to stimulus estimation. Because the HRF estimation is performed sequentially after stimulus estimation, its performance will inherit the patterns related to parameter changes and shown in Fig 5.6, 5.7, and 5.8, therefore not repeated here.

6

Experimental Data and Results

To further investigate the performance of this proposed estimating algorithm, in this chapter, experimental fUS data will be used as observation signals, and the results will be evaluated and discussed similarly as in Chapter 5. In Section 6.1, a pipeline that illustrates data pre-processing, as well as estimation steps, will be discussed. In Section 6.2, the estimated stimulus will be analyzed by comparing it with other methods and comparing performance among different trails. Then in Section 6.3, the HRF estimation results will be shown and evaluated.

6.1 Experimental Pipeline

The main differences between this experimental processing pipeline and the simulation in Chapter 5 are: (1) No data generation steps are needed; (2) More pre-processing is required to get the IVA-calculable observations $x_j(t)$. Therefore, in Figure 6.1, the blocks after getting $x_j(t)$ are the same as the ones in Figure 5.1, and as a result this section will focus on explaining the steps before getting $x_j(t)$.

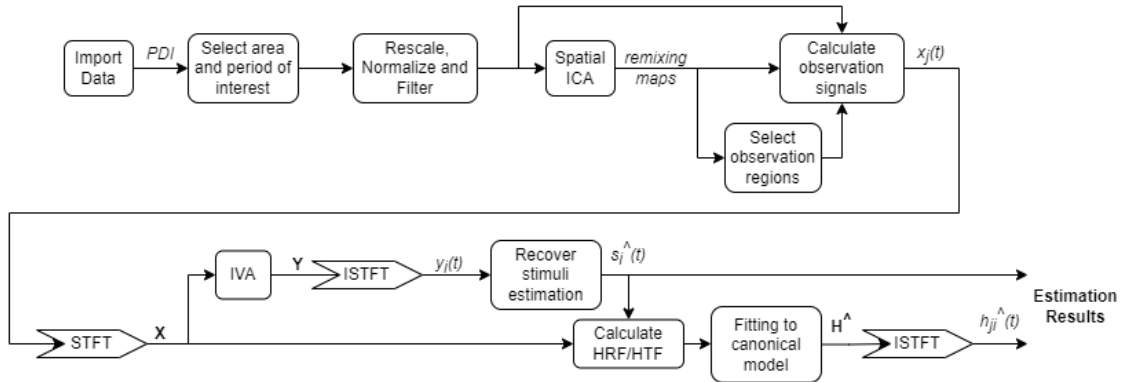


Figure 6.1: Experimental Pipeline

6.1.1 Data Description

The fUS dataset was recorded by CUBE research group from Erasmus MC. It is a PDI recording of a mouse's brain over time. In the experimental setting, there are two screens in front of the experiment object (mouse), one on the left and another on the right, which both display a series of icons that varies over time. A series of icons are displayed on each which differs in shape and size. Figure 6.2 shows all the icons used in this experiment and their corresponding index from 1 to 20. Each icon is repeated 10

times, and each time 3 seconds. The resting period is designed as a completely black screen, which is a random period between 5 to 9 seconds. The appearance of stimulus icons is also random.

In the rest of this chapter, we assume each different stimulus icon's appearance as a source signal, therefore, there are 20 different sources in total in this dataset. Since for this experiment, PDI is recorded continuously when different icons are displayed on screens, to extract the corresponding hemodynamic response we need to cut relative time series out of the whole PDI recording. This "cut and paste" step may lead to non-continuity inside extracted observation signal, but this effect can be reduced somehow by the temporal filtering step which will happen later.

Source	Left Screen	Right Screen	Source	Left Screen	Right Screen
	(1)	(6)		(11)	(16)
	(2)	(7)		(12)	(17)
	(3)	(8)		(13)	(18)
	(4)	(9)		(14)	(19)
	(5)	(10)		(15)	(20)

Figure 6.2: Stimuli icons in different sizes, shapes, and positions shown on screen.

As discussed in Chapter 2, the PDI recording is formed by averaging compound images over time. Here the fUS time series has the sampling frequency $F_s = 4.6503[Hz]$. The fUS data are stored as $(N_x \times N_y)$ time sequences, where N_x and N_y are the PDI image sizes along x and y axis. Therefore, the imported PDI here can be treated as observation signals in all $(N_x \times N_y)$ voxels.

Although the actual stimuli are part of the estimation targets (unknown) of this experiment, their true appearance patterns (ground truth) can be known from the experimental process which can be used for evaluation. To roughly visualize how the mouse's brain responds to each stimulus, 20 temporal correlation maps between all 20 stimulus series and the whole brain PDI voxel time series are generated and shown in Figure 6.3.

Each column of 5 maps represents stimuli of one certain shape and position and increases in size accordingly. It can be observed that, as icon size increases, the PDI brightness of certain regions which represents response amplitude also increases generally. The relation between the position (left or right) of the stimulus and the brain region with a higher response can also be observed, since the left stimulus will mostly

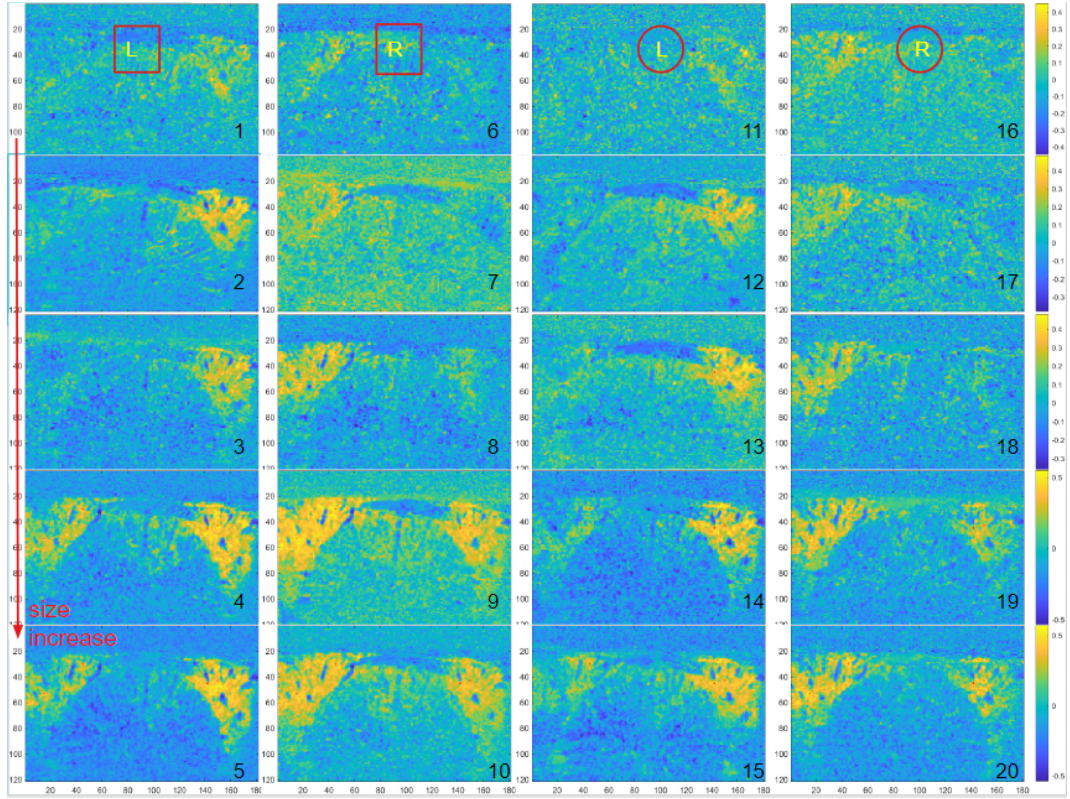


Figure 6.3: 20 different stimuli vary in position, symbol shape, and size.

receive a higher response from the right half of the brain, and vice versa.

6.1.2 Data Pre-processing

The raw PDI data acquired from fUS cannot be directly applied to the same pipeline as simulation data, because of the large voxel number, the noise, etc. Several pre-processing steps are needed to convert the PDI into desired $x_j(t)$.

There are two main steps in data pre-processing after importing PDI. The first is **selecting area and period of interest**. By cutting off edges with no useful information, the total data size can be reduced, therefore the image dimensions changed to $(N_{x_0} \times N_{y_0})$, where $N_{x_0} \leq N_x$ and $N_{y_0} \leq N_y$. Here N_{x_0} and N_{y_0} are the new voxel dimensions of the slice. To select several sources for analysis which is less than 20, the time periods when sources of interest are happening also need to be extracted. We use $N = 2$ source for this chapter, and source index 4 (Left, Square, Size 4) and 9 (Right, Square, Size 4) will be used as an example to show estimation performance regarding stimulus position. The extracted sources are shown in Figure 6.4, which can be used later to evaluate stimulus estimation.

The second step is to **rescale, normalize and filter**. To rescale the extracted PDI signals, we can treat the PDI image at each time point separately, and by dividing each voxel value with the mean value across the whole image at one moment, a rescaled *relative PDI* image is generated. For each relative PDI image, the relative values

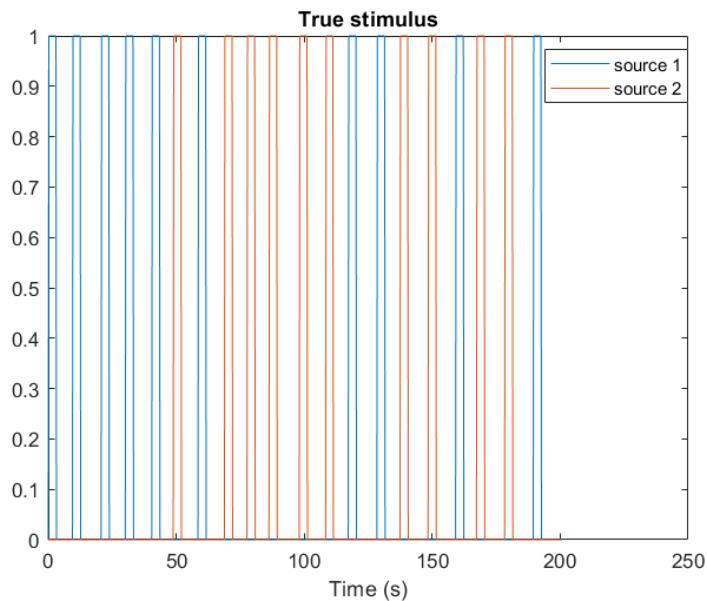


Figure 6.4: Sources with index 4 and 9

of voxels are maintained at a similar scale across time; while the amplitude behavior across the image is also preserved since a larger amplitude voxel will always have a larger relative value after rescaling. This is used to mitigate the potential global change in amplitude level which happen across time. Then, to normalize the PDI signals, the temporal mean of each voxel is subtracted from the original signal and then divided by their temporal standard deviations. Finally, a low-pass filter with a cut-off frequency at 0.2 [Hz] is applied to each voxel, so that noises can be mostly mitigated, which is similar to the denoising step in the simulation pipeline.

Now, the updated PDI consists of $(N_{x_0} \times N_{y_0})$ time sequences which are the hemodynamic response to source indexes 4 and 9. The voxel numbers is around 17k and time points is around 1k.

6.1.3 Spatial ICA and Region Selection

The PDI at the current stage usually has a larger number of voxels than the number of time points. To reduce the total number of observation signals, voxels need to be parcellated together into regions. This can be implemented using **Spatial ICA**(sICA), as already introduced in Chapter 4. The whole brain activity can be treated as a superposition of smaller independent brain activity patterns which happen in different volumetric regions, and as a result, the voxels \mathbf{v} here are labels of time sequences, which makes spatial independence analysis possible. The ICA model can be expressed as [50]:

$$B(\mathbf{v}, t) = \sum_{r=1}^R M_r(t) C_r(\mathbf{v}) \quad (6.1)$$

where $\mathbf{v} \in \mathbb{R}^2$ is the voxel location on the slice; R is the total number of independent patterns; $C_r(\mathbf{v})$ is the spatial activity map with size $(N_{x0} \times N_{y0})$; $M_r(t) \in \mathbb{R}^T$ is the corresponding activity time course. Since $C(\mathbf{v})$ here represents the spatial map of different activities, it can be used to generate R parcelled regions which we are interested in. By taking the inverse of each spatial map, the parcelization maps $D(\mathbf{v})$ can be generated for each independent activity, which indicates how to weigh the whole brain activity at each voxel to form parcelled regions.

After getting R parcelization maps of voxels, a manual **selection of observation regions** is needed to pick several most informative maps, in order to further reduce the total number of "observations", as well as concentrate on meaningful parcelization maps which reflects the regional behavior of the whole brain under certain stimuli. This step can be assisted by the known brain atlas as introduced in Chapter 2, where we can know which brain regions are corresponding to visual activities. In this example where $R = 30$, 5 maps can be manually selected as informative regions, as shown in the first row in Figure 6.5, while other maps are generally noisy or not meaningful according to the brain atlas.

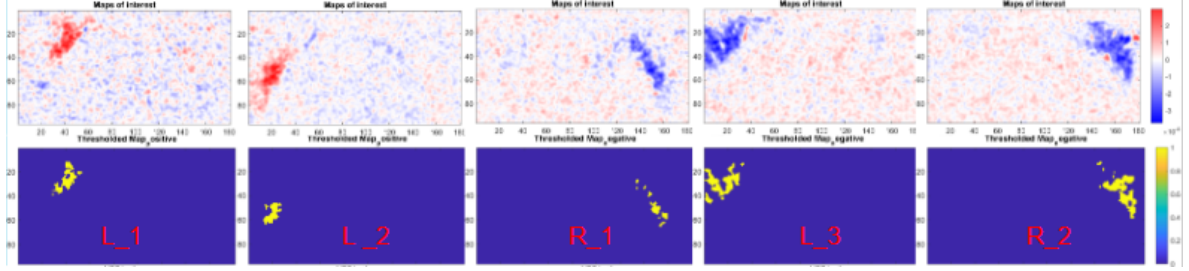


Figure 6.5: Selected parcelization maps and regions after thresholding.

To further process these maps and find brain regions that can be treated as regions of interest for observation signals, a threshold is needed for each map. Here the threshold is set to be at the first 1/4 highest value of parcelization map, and after thresholding, the selected regions of each map can also be shown in the second row of Figure 6.5 as yellow regions.

Now there are 5 regions of interest derived from brain activity maps, and the final step in this part is to **calculate observation signals** from these regions. Since the maps are $N_{x0} \times N_{y0}$ matrices with weighting coefficients as its entries, the calculation of signals should follow the weight given by the entries. Besides, since the summations of all entries within a region are not always equal to 1, a normalization is needed to unify each map's weighting scaling to be summed to 1. The process of calculating the j -th observation signal can be expressed as:

$$x_j(t) = \sum_{\mathbf{v} \in Region_{th,j}} D_j(\mathbf{v}) I(\mathbf{v}, t) \quad (6.2)$$

where $Region_{th,j}$ with $j = 1, \dots, 5$ represents one of the 5 selected thresholded regions; $D_j(\mathbf{v})$ is the spatial parcelization map; and $I(\mathbf{v}, t)$ is the PDI shown as time sequences.

Now all the pre-IVA processing are finished, and the rest steps are the same as simulation, only with a different observation number $M = 5$.

6.2 Stimulus Estimation

By using the proposed estimation algorithm, the stimulus estimation result of this example can be shown in Figure 6.6. Similar to the simulation result, here blue signals are estimated sources $y_i(t)$ by IVA, red circles indicate which peak will be recovered as an estimated stimulus, and yellow signals are scaled true stimuli for easier comparison. The cross-correlation evaluation gives a score of 0.8293, and the discrete score is 0.95.

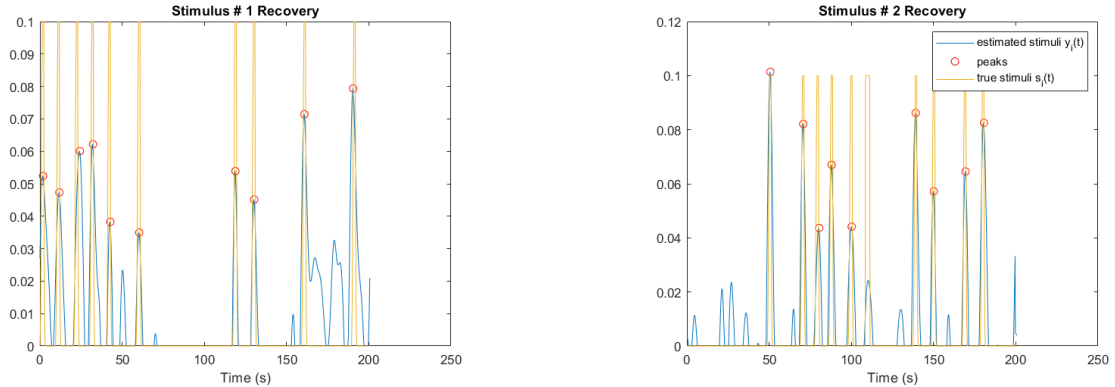


Figure 6.6: Experiment source estimation

6.2.1 Comparison with temporal ICA

One of IVA's advantages is that, compared with the traditional and widely-used temporal ICA (tICA) method to recover source stimulus, the IVA algorithm is based on the convolution model as stated in Eq. 4.3, while the temporal ICA method is based on a much simpler instantaneous mixing model assumption as expressed in Eq. 4.11. The goal of this comparison is to show that the convolutive model is important for stimulus reconstruction and stimuli can be estimated more accurately using this model assumption.

Figure 6.7 and 6.8 shown below compare both methods' stimulus peak estimation results, which is an important intermediate output before source estimation. In Figure 6.7, neither of the sources' peaks can be derived from temporal ICA separation results. While in Figure 6.8, the left subplot clearly shows that the peaks derived from IVA separation results can be used to recover source 1, and similarly, the right subplot can be used to derive source 2. Since for tICA, neither estimated results can be clearly assigned to corresponding true sources for cross-correlation evaluation, here the second evaluation method shown in Eq. 4.29 will be used. The "hit" tolerance is set to be a single stimulus activation duration. Using this evaluation equation, tICA will have a score of 0.3 out of 1, while the score of IVA is approximately 1.

Using the same evaluation equation in Eq. 4.29, a comparison between IVA and tICA among all pair of sources can be shown in Fig. 6.9. It can be observed that IVA achieves a generally better stimulus separation performance compared with tICA.

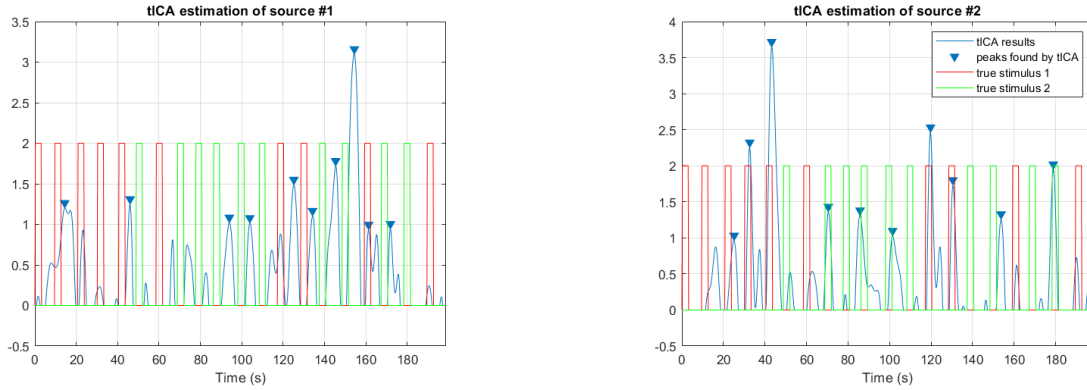


Figure 6.7: Temporal ICA stimulus peaks estimation results

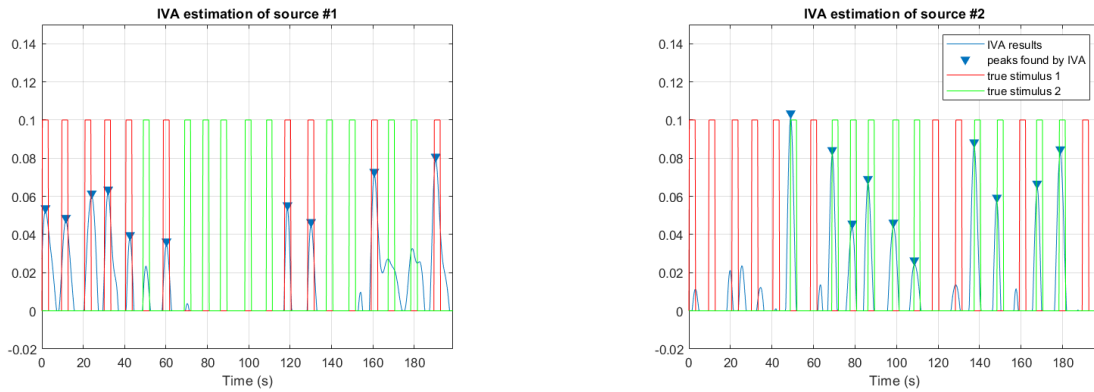


Figure 6.8: IVA stimulus peaks estimation results

6.2.2 Source Position Estimation Result

To further focus on estimating sources distinguished by position (icon shown on the left or right screen), 10 pairs of tests can be formed as shown in Table 6.1, and by applying the experiment pipeline steps on all of these trials, we can calculate evaluation score for each trail. As mentioned before, the stimulus estimation results are evaluated using cross-correlation between results and the true sources as expressed in Eq.4.28.

The first test between stimulus indexes 1 and 6 doesn't generate results due to poor performance. The estimated results are not comparable to either true source, therefore an evaluation score cannot be calculated. The rest of the tests are evaluated in score values (unit = 1). From the table, we can observe that square stimuli have a generally better performance than circle tests, and stimuli with a larger icon will have a better performance compared with a smaller one. However, this relation is not strictly linear, because each trial's performance may also be influenced by other factors, like test subject's tiredness or memory. Also, the example we chose in the previous explanations (source index 4 and 9) is the best case regarding source estimation among all other pairs.

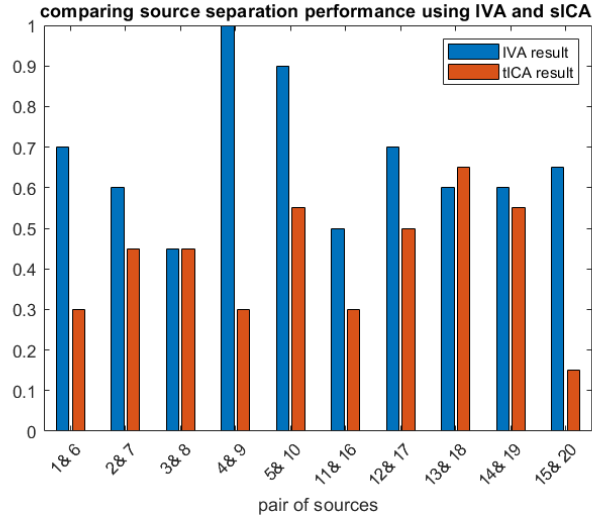


Figure 6.9: Performance comparison between IVA and tICA

Table 6.1: Stimulus Estimation score for different pair of sources.

Stimulus Index (<i>Square</i>)	Score	Stimulus Index (<i>Circle</i>)	Score
1, 6	N/A	11, 16	0.4053
2, 7	0.4859	12, 17	0.4865
3, 8	0.5601	13, 18	0.5902
4, 9	0.8293	14, 19	0.5681
5, 10	0.7802	15, 20	0.5450

As a comparison in literature, another thesis using the same dataset as this thesis also performs an estimation of stimulus [51]. One of its goals is to predict if the stimulus appears on the left or right screen. It uses the second stimulus estimation method as stated in Section 4.3.2, and the best result comes from the sparse dictionary learning (sDL) method, which is 0.87. It is higher than the best case as shown in Table 6.1. However, the worst case of this data-driven algorithm will have a score of around 0.5 (random guess), due to its classification nature. While for the IVA estimation, the worst case can reach a score of 0 when none of the peaks are recognized.

6.3 HRF Estimation

The HRF results can also be calculated following the experimental pipeline. One pair of HTF/HRF estimation results is shown as Figure 6.10 (for region R_1 and the 1st stimulus). Different from the plot of simulation HRF results, since in the experiment scenario the true HRFs (ground truth) are known, here the blue lines represent HRFs calculated using true sources, which can be referred to as an upper bound of estimation results. The red lines represent HTF/HRF estimation results without fitting, and the yellow lines represent fitted results. Due to HRF's physical properties, the length of the shown HRF result is trimmed to 10s.

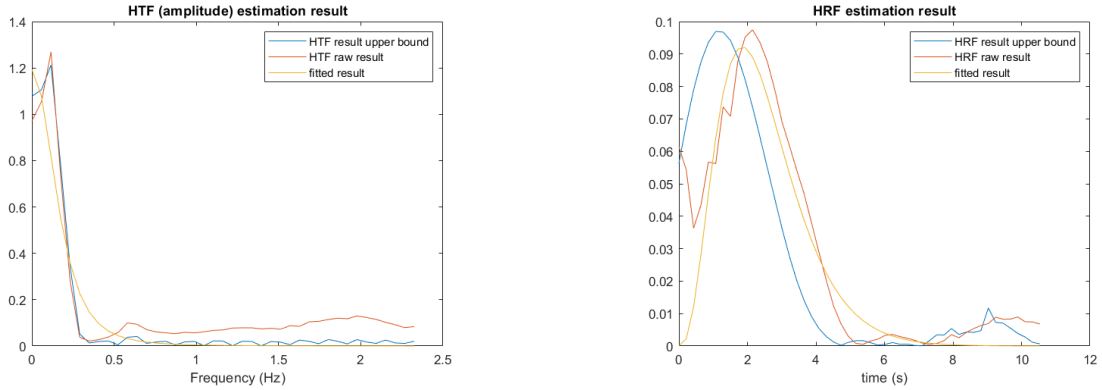


Figure 6.10: Estimation results for HTF and HRF

6.3.1 Evaluation

To evaluate HRF results without knowing the true HRFs, the second method mentioned in section 4.4.4 can be applied here. According to the Divided Visual Field Paradigm, a stimulus that appears in the left visual field will lead to a higher response in the right cerebral hemisphere, and the right stimulus will cause a higher response in the left hemisphere. Since one of the most important HRF characteristics is its amplitude, it can represent the level of response: a larger HRF amplitude means a higher response level.

Using the information mentioned above, HRF results of all $M = 5$ observations regions to $N = 2$ stimuli sources can be shown in figure 6.11. The first row is observation maps which also indicate their most activated brain regions (left or right). The second row is HRF estimation results corresponding to the first source (stimulus index 4, left screen), and the third row shows results for the second source (stimulus index 9, right screen). The number marked in each HRF plot is the amplitude value. The significantly larger one within each pair is written in red, and the values from unsatisfying results are marked in braces.

The two chosen stimuli icons have the same size and shape and only differ in position (left screen or right screen). Therefore, the source amplitudes of both stimuli can be assumed equal. And as a result, the level of response can be reflected through HRF amplitude, and compared with each other. Here HRF length of all results is trimmed to 10s.

It can be seen that in this example, both right brain observation regions R_1 and R_2 have a higher response to the left stimulus. For the left brain observation regions, two out of three HRF results show a higher response to the right stimulus, while for region L_1 both stimuli are having a similar level, therefore not very distinguishable. In conclusion, in this 5-by-2 HRF test, a $4/5 = 80\%$ correctness is achieved.

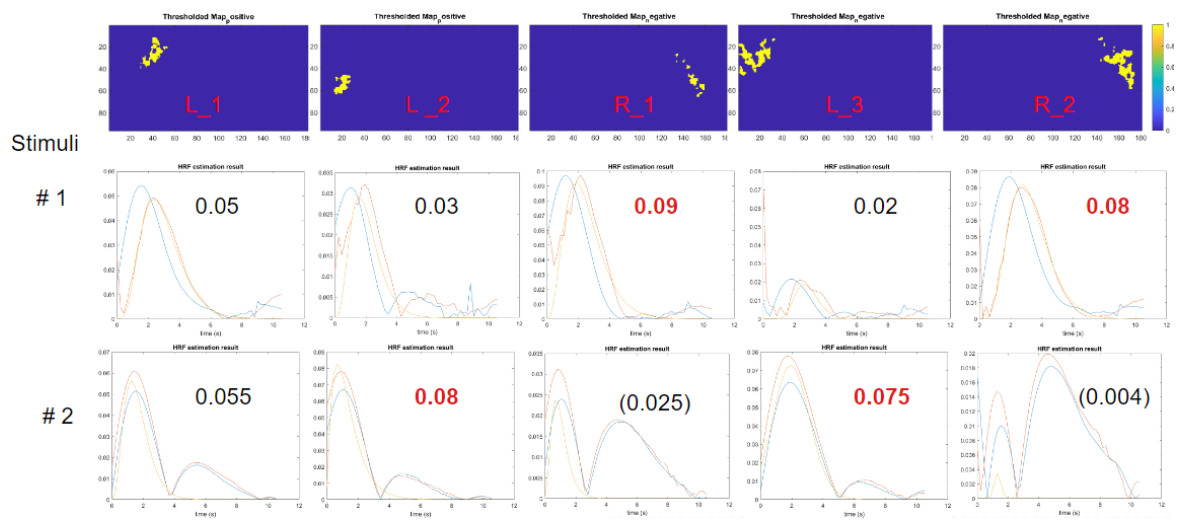


Figure 6.11: HRF results shown by observation region and stimulus position pairs.

In this chapter, the research questions raised in Chapter 1 will be first answered accordingly in section 7.1. Although the results shown in previous chapters demonstrate a desirable performance, there are still drawbacks that exist in this proposed estimation process regarding the current research problem. The proposed method will be critically discussed from two aspects: its limitations and potential aspects for future improvement. In Section 7.2, limitations regarding the estimation algorithm's assumption, methodology, and results generation will be explained. Then based on these limitations, in section 7.3, several possible directions for future work are proposed.

7.1 Answers to Research Questions

In Chapter 1, there are three research questions raised for this thesis. Corresponding answers and explanations will be given here:

- **RQ1:** How to convert the signal estimation problem into frequency domain?

ANS1: In this thesis STFT is used to convert the signal estimation problem into frequency domain. As a result, IVA algorithm can achieve STFT coefficient vectors separation across all frequency bins.

- **RQ2:** What frequency domain technique can be considered in solving this estimation problem?

ANS2: First ICA is considered for stimulus separation, then IVA is found to be its suitable higher dimension extension for this estimation problem. The ideal goal is to achieve stimulus and HRF separation simultaneously, while the attempt failed due to the erroneous HRF results. Therefore, a sequential method is chosen for HRF estimation after acquiring stimulus results.

- **RQ3:** What neuroscientific insights can the estimation results give?

ANS3: The experimental analysis in this thesis proves that convolutive model assumption is more accurate than instantaneous mixing model. It is done by comparing the stimulus estimation results between IVA and tICA results. The HRF estimation results also indicates the hemodynamic response level difference between left and right hemisphere when exposed to visual stimulus in left/right visual fields. However, since the dataset and the corresponding settings are limited, these insights still require further proof to be applied generally.

7.2 Limitations

From the answers to the research question as well as the proposed algorithm itself, we can see that this method explained so far still has several limitations:

(1) **Prior source PDF is not exactly super-Gaussian.** In section 4.2.2, when explaining the learning algorithm used in IVA, the source prior PDF information is used for constructing score functions $\phi(\mathbf{y}_i^f)$ as expressed in Equation 4.26. Currently, there's little literature investigating the actual prior PDF of neuro-signal stimulus, therefore, it is assumed that stimulus source signals will have super-Gaussian distribution in the frequency domain, which is a conclusion from audio signal research and used here for simplicity. Although IVA can still be successfully performed on neuro-signals using this super-Gaussian prior PDF, the estimation performance may be compromised due to this context mismatch.

(2) **Applicable scenarios and settings are limited.** As described in Section 5.2.1, there are several parameters that will influence the estimation performance, such as the number of observations and sources, rest time, and SNR level. While in real cases, the values of these parameters are not always the "best" choices. Therefore, the estimation performance's upper bound will be affected. This can also be observed in Table 6.1, where different pairs which differ in appearance order, size, and shape will have different performances, which is reasonable but still requires further investigation.

(3) **Noise model is too simplistic.** Here we only consider additive white noise in the signal model, while the real noise and artifacts in the fUS signal are far more complex than that [52]. There are different noise sources that can come from physiological, thermal, and also motion-related behaviors. Therefore, after simply de-noising additive white noises, there will still be artifacts that remained in the signal data.

7.3 Future Work

Based on the previous discussion of methodology and limitations, several directions of future work can be proposed as follows:

(1) To reduce the influence of inaccurate prior source PDF, more research regarding neural stimulus' frequency domain property can be conducted. It can be realized by designing source stimuli with a certain pattern, which not only has a prior PDF that can be expressed easily, but also can lead to better performance with this method. In this case, the multivariate score function can also be chosen more accurately.

(2) To further investigate the most suitable scenarios where this method is applicable, more simulations and experiments with various settings can be performed. It can also help validate assumptions like certain properties of neural signals and the capability of this IVA algorithm.

(3) A more complex noise model can be used in simulation and experimental fUS processing. And as a result, corresponding de-noising algorithms should be performed in addition. The noise model can be chosen based on the experimental paradigm in which certain influencing factors can be ignored by choice, such as thermal artifacts which can be treated as a constant through a short experiment. While other factors that are related should be kept.

(4) The *Revised Simultaneous method* can be further improved by utilizing HRF information which is acquired afterward so that the estimation result can be improved in an iterative way. Since the IVA algorithm only assume there is a certain filter existing in each mixing process, the information about the filter itself (in this case, HTF) is not used fully, which leads to a sub-optimal result. Although the attempt as mentioned in 4.4.2 failed, this IVA algorithm still holds the potential to be improved better so that stimulus and HRF can be estimated together in one step, rather than sequentially.

(5) Since the dataset used in Chapter 6 is segmented and connected again to form corresponding observation signals, the non-continuity caused by this step may lead to a larger error during estimation. Therefore, a more suitable experiment for this proposer estimation method can be designed in the future.

Conclusion

In this thesis paper, a joint estimation method is proposed for both HRF and stimulus using fUS data.

In the first chapter, an introduction is given about fUS imaging and the hemodynamic system. The thesis research problem consists of three parts: how to convert the context into frequency domain; what technique can be used; what insights can be found from this estimation.

In the second chapter, background information is given regarding three topics. The fUS technique and PDI imaging process are explained. Then, brain mapping is introduced, which provides this estimation problem with a broader context. An illustration of the concerned hemodynamic signals is also shown in this chapter.

In the third chapter, literature related to HRF and stimulus estimation, as well as audio signal application which shares a similar signal mixing model are discussed. For the time domain hemodynamic analysis, HRF canonical model and GLM method are two of the most popular choices. There's also a data-driven approach that provides a more flexible scheme for signal estimation. For frequency domain analysis, there's not so much related work, which provides space for more new developments. Then by discussing the audio signal analysis problem, ICA is found to be a potential method for further investigation.

In the fourth chapter, the main steps and techniques used in the proposed estimation algorithm are explained in detail. First, the estimation problem itself is explained using equations for signal modeling and domain transformation. Most notations and symbols involved in the algorithm are also introduced there. Then ICA and its frequency domain application attempt are explained, which leads to the conclusion that the permutation problem is not what we desired. Therefore, IVA which shares a similar essence with ICA is introduced, which avoids the aforementioned permutation problem, and can provide frequency domain solution in a more direct way. Then the detailed steps in the IVA algorithm are explained, as well as additional steps needed after IVA to achieve stimulus and HRF estimation. Finally, HRF and HTF Gamma model is introduced, which will be used later in the result fitting step.

In the fifth chapter, artificial data is generated for simulation. Then an example setting is used to generate results using the proposed pipeline. In this 2-source 3-observation example, IVA is used first to find stimulus peaks when activation happens. Then by reconstructing the source signal, stimulus estimation is achieved. HRF estimation and final fitting are done after acquiring stimulus results, which leads to a sequential method. The estimation results here are displayed and evaluated separately. Quantitative scores are given to the evaluation, from which we can see that this simulation example has satisfying performance.

In the sixth chapter, experimental data provided by Erasmus MC is used for analysis. First, the dataset itself is introduced, which leads to the example that will be used

throughout this chapter. Then by applying the experimental pipeline to the dataset, each step along the way is explained together with visualized results. The sICA method is used for pre-processing the dataset, which can reduce voxel dimension and create regions of interest in the fUS image. Then by constructing observation time courses, IVA can be applied to the response signals, which leads to final estimation results. The stimulus estimation result is shown and compared with the tICA result, which is based on an instantaneous mixture assumption. The comparison shows that IVA achieves a much better estimation of stimulus compared with tICA. Since the example only shows the results of one pair of stimuli, another table is used to show the general source estimation performance of all 10 stimulus pairs. From the evaluation scores, we can conclude that this algorithm's performance may highly rely on suitable experimental settings, since some pairs have very good performance while others don't. Finally, the HRF results are also shown and evaluated, which takes advantage of the Divided visual Field Paradigm for result validation. The result shows that the HRF amplitude result follows our assumption with an 80% correctness, although there are still a few results that don't perform as expected.

In the seventh chapter, first researches questions are answered based on all the previous chapters. Then several limitations of the current work are listed, which critically explained the drawbacks of some techniques and experimental designs. According to the limitations and inspirations from previous chapters, several potential future working directions are also listed as a reference.

In conclusion, this thesis provides a solution to the concerned research questions. This proposed estimation approach gives satisfying results for both stimulus and HRF estimation using frequency domain methods under suitable experimental design. It also provides valuable insights into the convolution hemodynamic signal system, which may benefit researchers who are interested in neuroscience and ICA/IVA-related topics.

Bibliography

- [1] L.-A. Sieu, A. Bergel, E. Tiran, T. Deffieux, M. Pernot, J.-L. Gennisson, M. Tanter, and I. Cohen, “Eeg and functional ultrasound imaging in mobile rats,” *Nature methods*, vol. 12, no. 9, pp. 831–834, 2015.
- [2] J. C. Gore *et al.*, “Principles and practice of functional mri of the human brain,” *The Journal of clinical investigation*, vol. 112, no. 1, pp. 4–9, 2003.
- [3] L.-D. Liao, V. Tsytsarev, I. Delgado-Martínez, M.-L. Li, R. Erzurumlu, A. Vipin, J. Orellana, Y.-R. Lin, H.-Y. Lai, Y.-Y. Chen *et al.*, “Neurovascular coupling: in vivo optical techniques for functional brain imaging,” *Biomedical engineering online*, vol. 12, no. 1, pp. 1–20, 2013.
- [4] E. Mace, G. Montaldo, B.-F. Osmanski, I. Cohen, M. Fink, and M. Tanter, “Functional ultrasound imaging of the brain: theory and basic principles,” *IEEE Transactions on Ultrasonics, Ferroelectrics, and Frequency Control*, vol. 60, no. 3, pp. 492–506, 2013.
- [5] J. Robin, R. Rau, B. Lafci, A. Schroeter, M. Reiss, X.-L. Deán-Ben, O. Goksel, and D. Razansky, “Hemodynamic response to sensory stimulation in mice: Comparison between functional ultrasound and optoacoustic imaging,” *NeuroImage*, vol. 237, p. 118111, 2021.
- [6] T. Deffieux, C. Demene, M. Pernot, and M. Tanter, “Functional ultrasound neuroimaging: a review of the preclinical and clinical state of the art,” *Current opinion in neurobiology*, vol. 50, pp. 128–135, 2018.
- [7] E. Macé, G. Montaldo, I. Cohen, M. Baulac, M. Fink, and M. Tanter, “Functional ultrasound imaging of the brain,” *Nature methods*, vol. 8, no. 8, pp. 662–664, 2011.
- [8] N. Kriegeskorte, R. Goebel, and P. Bandettini, “Information-based functional brain mapping,” *Proceedings of the National Academy of Sciences*, vol. 103, no. 10, pp. 3863–3868, 2006.
- [9] T. L. Gilbert, “The allen brain atlas as a resource for teaching undergraduate neuroscience,” *Journal of Undergraduate Neuroscience Education*, vol. 16, no. 3, p. A261, 2018.
- [10] M. T. Banich, “The divided visual field technique in laterality and interhemispheric integration,” in *Experimental methods in neuropsychology*. Springer, 2003, pp. 47–63.
- [11] V. J. Bourne, “The divided visual field paradigm: Methodological considerations,” *Laterality*, vol. 11, no. 4, pp. 373–393, 2006.
- [12] R. B. Ivry, L. C. Robertson, and L. C. Robertson, *The two sides of perception*. MIT press, 1998.

- [13] K. J. Worsley and K. J. Friston, “Analysis of fmri time-series revisited—again,” *Neuroimage*, vol. 2, no. 3, pp. 173–181, 1995.
- [14] A. M. Wink and J. B. T. M. Roerdink, “Extracting the haemodynamic response function from fmri time series using fourier-wavelet regularised deconvolution with orthogonal spline wavelets,” in *2006 14th European Signal Processing Conference*, 2006, pp. 1–5.
- [15] M. A. Lindquist and T. D. Wager, “Validity and power in hemodynamic response modeling: a comparison study and a new approach,” *Human brain mapping*, vol. 28, no. 8, pp. 764–784, 2007.
- [16] H. Cherkaoui, T. Moreau, A. Halimi, C. Leroy, and P. Ciuciu, “Multivariate semi-blind deconvolution of fmri time series,” *NeuroImage*, vol. 241, p. 118418, 2021.
- [17] V. A. Vakorin, R. Borowsky, and G. E. Sarty, “Characterizing the functional mri response using tikhonov regularization,” *Statistics in medicine*, vol. 26, no. 21, pp. 3830–3844, 2007.
- [18] J. Ollinger, G. L. Shulman, and M. Corbetta, “Separating processes within a trial in event-related functional mri: I. the method,” *Neuroimage*, vol. 13, no. 1, pp. 210–217, 2001.
- [19] I. Khalidov, J. Fadili, F. Lazeyras, D. Van De Ville, and M. Unser, “Activelets: Wavelets for sparse representation of hemodynamic responses,” *Signal processing*, vol. 91, no. 12, pp. 2810–2821, 2011.
- [20] K. J. Friston, O. Josephs, G. Rees, and R. Turner, “Nonlinear event-related responses in fmri,” *Magnetic resonance in medicine*, vol. 39, no. 1, pp. 41–52, 1998.
- [21] K. J. Friston, A. P. Holmes, K. J. Worsley, J.-P. Poline, C. D. Frith, and R. S. Frackowiak, “Statistical parametric maps in functional imaging: a general linear approach,” *Human brain mapping*, vol. 2, no. 4, pp. 189–210, 1994.
- [22] M. A. Lindquist, J. M. Loh, L. Y. Atlas, and T. D. Wager, “Modeling the hemodynamic response function in fmri: efficiency, bias and mis-modeling,” *Neuroimage*, vol. 45, no. 1, pp. S187–S198, 2009.
- [23] J.-B. Poline and M. Brett, “The general linear model and fmri: does love last forever?” *Neuroimage*, vol. 62, no. 2, pp. 871–880, 2012.
- [24] G. H. Glover, “Deconvolution of impulse response in event-related bold fmri1,” *Neuroimage*, vol. 9, no. 4, pp. 416–429, 1999.
- [25] P. Ciuciu, J.-B. Poline, G. Marrelec, J. Idier, C. Pallier, and H. Benali, “Unsupervised robust nonparametric estimation of the hemodynamic response function for any fmri experiment,” *IEEE Transactions on medical imaging*, vol. 22, no. 10, pp. 1235–1251, 2003.

- [26] F. Pedregosa, M. Eickenberg, P. Ciuciu, B. Thirion, and A. Gramfort, “Data-driven hrf estimation for encoding and decoding models,” *NeuroImage*, vol. 104, pp. 209–220, 2015.
- [27] G.-R. Wu, W. Liao, S. Stramaglia, J.-R. Ding, H. Chen, and D. Marinazzo, “A blind deconvolution approach to recover effective connectivity brain networks from resting state fmri data,” *Medical image analysis*, vol. 17, no. 3, pp. 365–374, 2013.
- [28] H. Cherkaoui, T. Moreau, A. Halimi, and P. Ciuciu, “Sparsity-based blind deconvolution of neural activation signal in fmri,” in *ICASSP 2019-2019 IEEE International Conference on Acoustics, Speech and Signal Processing (ICASSP)*. IEEE, 2019, pp. 1323–1327.
- [29] D. Rio, R. Rawlings, L. Woltz, J. Gilman, D. Hommer *et al.*, “Analysis of fmri single subject data in the fourier domain acquired using a multiple input stimulus experimental design,” *Journal of Signal and Information Processing*, vol. 3, no. 04, p. 469, 2012.
- [30] J. L. Marchini and B. D. Ripley, “A new statistical approach to detecting significant activation in functional mri,” *NeuroImage*, vol. 12, no. 4, pp. 366–380, 2000.
- [31] S. Makino, H. Sawada, R. Mukai, and S. Araki, “Blind source separation of convolutive mixtures of speech in frequency domain,” *IEICE transactions on fundamentals of electronics, communications and computer sciences*, vol. 88, no. 7, pp. 1640–1655, 2005.
- [32] A. I. Koutrouvelis, R. C. Hendriks, R. Heusdens, and J. Jensen, “Robust joint estimation of multimicrophone signal model parameters,” *IEEE/ACM Transactions on Audio, Speech, and Language Processing*, vol. 27, no. 7, pp. 1136–1150, 2019.
- [33] W. Wang, S. Sanei, and J. A. Chambers, “Penalty function-based joint diagonalization approach for convolutive blind separation of nonstationary sources,” *IEEE Transactions on Signal Processing*, vol. 53, no. 5, pp. 1654–1669, 2005.
- [34] T. Kim, H. T. Attias, S.-Y. Lee, and T.-W. Lee, “Blind source separation exploiting higher-order frequency dependencies,” *IEEE transactions on audio, speech, and language processing*, vol. 15, no. 1, pp. 70–79, 2006.
- [35] S.-i. Amari, “Natural gradient works efficiently in learning,” *Neural Computation*, vol. 10, no. 2, pp. 251–276, 1998.
- [36] A. J. Bell and T. J. Sejnowski, “An information-maximization approach to blind separation and blind deconvolution,” *Neural Computation*, vol. 7, no. 6, pp. 1129–1159, 1995.
- [37] A. Hyvarinen, “Fast and robust fixed-point algorithms for independent component analysis,” *IEEE Transactions on Neural Networks*, vol. 10, no. 3, pp. 626–634, 1999.

- [38] V. D. Calhoun, J. Liu, and T. Adalı, “A review of group ica for fmri data and ica for joint inference of imaging, genetic, and erp data,” *Neuroimage*, vol. 45, no. 1, pp. S163–S172, 2009.
- [39] F. I. Karahanoglu and D. Van De Ville, “Transient brain activity disentangles fmri resting-state dynamics in terms of spatially and temporally overlapping networks,” *Nature communications*, vol. 6, no. 1, pp. 1–10, 2015.
- [40] M. Gholamrezai, M. R. Aghabozorgi, and H. R. Abutalebi, “Blind separation of speech target sources using ica in the frequency domain,” in *2010 5th International Symposium on Telecommunications*. IEEE, 2010, pp. 765–768.
- [41] J. Anemüller, T. J. Sejnowski, and S. Makeig, “Complex independent component analysis of frequency-domain electroencephalographic data,” *Neural networks*, vol. 16, no. 9, pp. 1311–1323, 2003.
- [42] H. W. Kuhn, “The hungarian method for the assignment problem,” *Naval research logistics quarterly*, vol. 2, no. 1-2, pp. 83–97, 1955.
- [43] A. Ciaramella, R. Tagliaferri, and M. Funaro, “Separation of convolved mixtures in frequency domain ica,” in *International Mathematical Forum*, vol. 16. Citeseer, 2006, pp. 769–795.
- [44] J.-H. Lee, T.-W. Lee, F. A. Jolesz, and S.-S. Yoo, “Independent vector analysis (iva): multivariate approach for fmri group study,” *Neuroimage*, vol. 40, no. 1, pp. 86–109, 2008.
- [45] I. Lee, T. Kim, and T.-W. Lee, “Fast fixed-point independent vector analysis algorithms for convolutive blind source separation,” *Signal Processing*, vol. 87, no. 8, pp. 1859–1871, 2007.
- [46] T. Kim, I. Lee, and T.-W. Lee, “Independent vector analysis: definition and algorithms,” in *2006 Fortieth Asilomar Conference on Signals, Systems and Computers*. IEEE, 2006, pp. 1393–1396.
- [47] L. D. Lewis, K. Setsompop, B. R. Rosen, and J. R. Polimeni, “Stimulus-dependent hemodynamic response timing across the human subcortical-cortical visual pathway identified through high spatiotemporal resolution 7t fmri,” *Neuroimage*, vol. 181, pp. 279–291, 2018.
- [48] S. Van Eyndhoven, B. Hunyadi, L. De Lathauwer, and S. Van Huffel, “Flexible fusion of electroencephalography and functional magnetic resonance imaging: Revealing neural-hemodynamic coupling through structured matrix-tensor factorization,” in *2017 25th European Signal Processing Conference (EUSIPCO)*. IEEE, 2017, pp. 26–30.
- [49] A. Erol, S. Van Eyndhoven, S. Koekkoek, P. Kruizinga, and B. Hunyadi, “Joint estimation of hemodynamic response and stimulus function in functional ultrasound using convolutive mixtures,” in *2020 54th Asilomar Conference on Signals, Systems, and Computers*. IEEE, 2020, pp. 246–250.

- [50] I. Daubechies, E. Roussos, S. Takerkart, M. Benharrosh, C. Golden, K. D'ardenne, W. Richter, J. D. Cohen, and J. Haxby, "Independent component analysis for brain fmri does not select for independence," *Proceedings of the National Academy of Sciences*, vol. 106, no. 26, pp. 10 415–10 422, 2009.
- [51] M. Enthoven, "Differentiating task-based functional ultrasound signals via data-driven decompositions," 2021.
- [52] E. Uruñuela, T. A. W. Bolton, D. Van De Ville, and C. Caballero-Gaudes, "Hemodynamic deconvolution demystified: Sparsity-driven regularization at work," 2021. [Online]. Available: <https://arxiv.org/abs/2107.12026>